Prediction of Falling Cylinder Through Air-Water-Sediment Columns

Peter C. Chu[1]

e-mail: chu@nps.navy.mil

Chenwu Fan

Naval Ocean Analysis and Prediction Laboratory,
Department of Oceanography,
Naval Postgraduate School,
Monterey, CA 93943

A falling rigid body through air, water, and sediment is investigated experimentally and theoretically. Two experiments were conducted to drop rigid cylinders with density ratio around 1.8 into shallow water (around 13 m deep) in the Monterey Bay (Exp-1) and into the Naval Postgraduate School's swimming pool (Exp-2). During the experiments, we carefully observe cylinder track and burial depth while simultaneously taking gravity cores (in Exp-1). After analyzing the gravity cores, we obtain the bottom sediment density and shear strength profiles. The theoretical work includes the development of a 3D rigid body impact burial prediction model (IMPACT35) that contains three components: triple coordinate transform and hydrodynamics of a falling rigid object in a single medium (air, water, or sediment) and in multiple media (air-water and water-sediment interfaces). The model predicts the rigid body's trajectory in the water column and burial depth and orientation in the sediment. The experimental data (burial depth, sediment density, and shear strength) show the capability of IMPACT35 in predicting the cylinder's trajectory and orientation in a water column and burial depth and orientation in sediment.
[DOI: 10.1115/1.2125975]

1 Introduction

Study on the movement of a rigid body in fluid has wide scientific significance and technical application. The scientific studies of the hydrodynamics of a rigid cylinder in fluid involve the nonlinear dynamics, flight theory, body-fluid interaction, and instability theory. The body forces include the gravity and the buoyancy force. The hydrodynamic forces include the drag and lift forces that depend on the fluid-to-body velocity and the impact force as the body penetrates the air-water or water-sediment interfaces. Usually, a nonlinear dynamical system is needed to predict a falling rigid body in fluid, e.g., [1].

Recently, the scientific problem about rigid body movement in the air-water-sediment columns drew attention to the naval research. This is due to the threat of mines in the naval operations. Within the past 15 years three U.S. ships, the *USS Samuel B. Roberts* (FFG-58), *Tripoli* (LPH-10), and *Princeton* (CG-59) have fallen victim to mines. Total ship damage was $125 million while the mines cost approximately $30,000 [2]. Mines have evolved over the years from the dumb "horned" contact mines that damaged the *Tripoli* and *Roberts* to ones that are relatively sophisticated—nonmagnetic materials, irregular shapes, anechoic coatings, multiple sensors, and ship count routines. Despite their increased sophistication, mines remain inexpensive and are relatively easy to manufacture, keep, and place. Water mines are characterized by three factors [3,4]: position in water (bottom, moored, rising, and floating), method of delivery (aircraft, surface, and subsurface), and method of actuation (acoustic and/or magnetic influence, pressure, contact, and controlled). Accurate mine burial predictions are inherently difficult to make because of uncertainties in both mine deployment conditions and the relevant environmental parameters [5]. The U.S. Navy developed opera-

tional models to predict the environmental parameters for mine burial prediction [6]. Recently, statistical methods such as the Monte Carlo method [7] and the expert system method [5] have been developed. These methods need a core-physical model for describing the movement of falling rigid body through air-water-sediment columns.

When the rigid body is cylindrical, this dynamical system can be simplified using three coordinate systems: earth-fixed coordinate (E-coordinate), cylinder's main-axis following coordinate (M-coordinate), and hydrodynamic force following coordinate (F-coordinate). The origin of both M- and F-coordinates is at the cylinder's center of mass (COM). The body forces and their moments are easily calculated using the E-coordinate system. The hydrodynamic forces and their moments are easily computed using the F-coordinate. The cylinder's moments of gyration are simply represented using the M-coordinate. Recently, Chu et al. [8] developed a recursive model to predict the cylinder's translation velocity and orientation in the water column (single phase) on the base of the triple coordinate transformation.

To extend the recursive model from single medium (water column) to multi-media (air, water, sediment), a falling cylinder through air-water and water-sediment interfaces (i.e., cylinder contacting with two media) should be particularly analyzed. The cylinder is decomposed into two parts with each one contacting one medium. For the air-water penetration, the cylinder is decomposed into air and water parts. For the water-sediment penetration, the cylinder is decomposed into water and sediment parts. The body forces (such as the buoyancy force) and surface forces (such as pressure and hydrodynamic force) are computed separately for the two parts. A fully three-dimensional model is developed for prediction of the translation velocity and orientation of falling rigid cylinder through air, water, and sediment. Theoretical model development and a cylinder drop experiment for the model evaluation are depicted in this paper.

The outline of this paper is as follows: Section 2 depicts the triple coordinate systems. Section 3 describes the dynamics for determining the cylinder's translation velocity and orientation. Section 4 presents the equivalent cylinder method for computing hydrodynamic forces and torques when the cylinder penetrates the air-water and water-sediment interfaces. Section 5 describes forces and torques in air and water. Section 6 describes the resis-
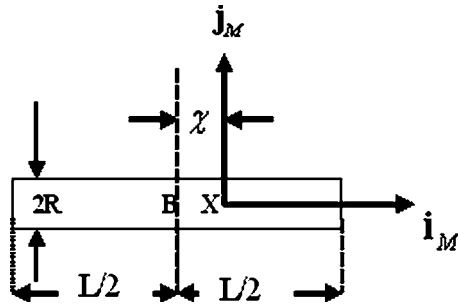

Fig. 1 M-coordinate with the COM as the origin X and (i_m, j_m) as the two axes. Here, χ is the distance between the COV (B) and COM (X), (L, R) are the cylinder's length and radius.

tance from sediments. Section 7 shows the model integration. Section 8 describes two cylinder drop experiments and observational data processing. Section 9 presents the model-data inter comparison. The conclusions are listed in Sec. 10.

2 Triple Coordinate Systems

Consider an axially symmetric cylinder with the centers of mass (COM) **X** [or called gravity center (GC) in literatures] and center of volume (COV) **B** on the main axis (Fig. 1). Let (L, R, χ) represent the cylinder's length, radius, and the distance between the two points $(\mathbf{X}, \mathbf{B})$. The positive χ values refer to nose-down case, i.e., the point **X** is lower than the point **B**. Three coordinate systems are used to model the falling cylinder through the air, water, and sediment phases: earth-fixed coordinate (E-coordinate), main-axis following coordinate (M-coordinate), and force following coordinate (F-coordinate) systems. All the systems are three-dimensional, orthogonal, and right-handed [8].

2.1 E-Coordinate. The E-coordinate is represented by $F_E(O, \mathbf{i}, \mathbf{j}, \mathbf{k})$ with the origin "O" and three axes: x, y axes (horizontal) with the unit vectors $(\mathbf{i}, \mathbf{j})$ and z axis (vertical) with the unit vector **k** (upward positive). The position of the cylinder is represented by the position of the COM,

$$\mathbf{X} = x\mathbf{i} + y\mathbf{j} + z\mathbf{k}, \tag{1}$$

which is translation of the cylinder. The translation velocity is given by

$$\frac{d\mathbf{X}}{dt} = \mathbf{V}, \quad \mathbf{V} = (u, v, w). \tag{2}$$

2.2 M-Coordinate. Let orientation of the cylinder's main axis (pointing downward) be given by $\mathbf{i}_M$. The angle between $\mathbf{i}_M$ and **k** is denoted by $\psi_2 + \pi/2$. Projection of the vector $\mathbf{i}_M$ onto the (x, y) plane creates angle (ψ_3) between the projection and the x axis (Fig. 2). The M-coordinate is represented by $F_M(\mathbf{X}, \mathbf{i}_M, \mathbf{j}_M, \mathbf{k}_M)$ with the origin "**X**", unit vectors $(\mathbf{i}_M, \mathbf{j}_M, \mathbf{k}_M)$, and coordinates (x_M, y_M, z_M). In the plane consisting of vectors $\mathbf{i}_M$ and **k** (passing through the point M), two new unit vectors $(\mathbf{j}_M, \mathbf{k}_M)$ are defined with $\mathbf{j}_M$ perpendicular to the $(\mathbf{i}_M, \mathbf{k})$ plane, and $\mathbf{k}_M$ perpendicular to $\mathbf{i}_M$ in the $(\mathbf{i}_M, \mathbf{k})$ plane. The unit vectors of the M-coordinate system are given by (Fig. 2)

$$\mathbf{j}_M = \mathbf{k}_M \times \mathbf{i}_M, \quad \mathbf{k}_M = \mathbf{i}_M \times \mathbf{j}_M. \tag{3}$$

The M-coordinate system is solely determined by orientation of the cylinder's main axis $\mathbf{i}_M$. Let the vector **P** be represented by $^E\mathbf{P}$ in the E-coordinate and by $^M\mathbf{P}$ in the M-coordinate, and let $_M^E\mathbf{R}$ be the rotation matrix from the M-coordinate to the E-coordinate,
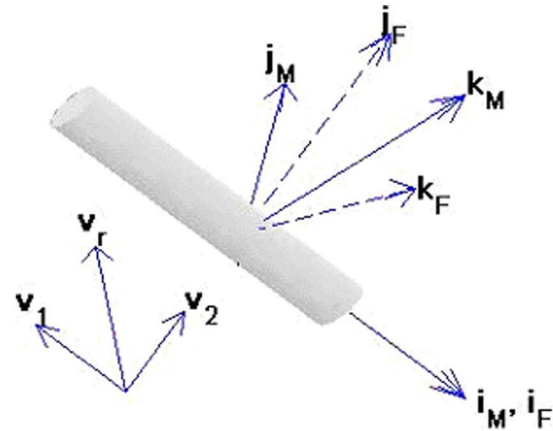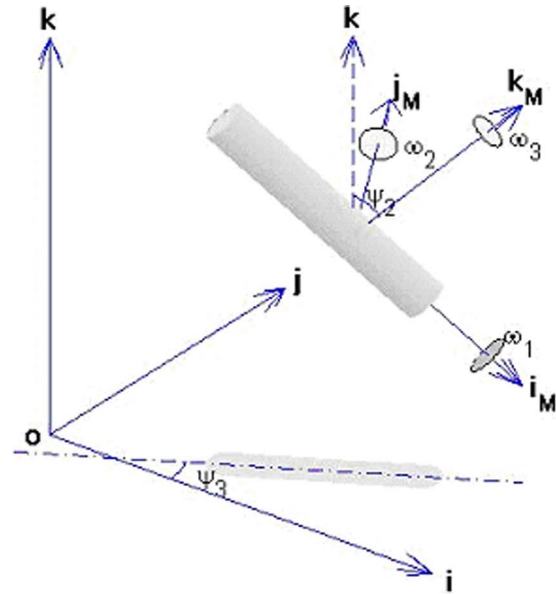

Fig. 2 Three coordinate systems

$$_M^E\mathbf{R}(\psi_2, \psi_3) \equiv \begin{bmatrix} r_{11} & r_{12} & r_{13} \\ r_{21} & r_{22} & r_{23} \\ r_{31} & r_{32} & r_{33} \end{bmatrix} = \begin{bmatrix} \cos\psi_3 & -\sin\psi_3 & 0 \\ \sin\psi_3 & \cos\psi_3 & 0 \\ 0 & 0 & 1 \end{bmatrix}$$
$$\times \begin{bmatrix} \cos\psi_2 & 0 & \sin\psi_2 \\ 0 & 1 & 0 \\ -\sin\psi_2 & 0 & \cos\psi_2 \end{bmatrix}, \tag{4}$$

which represents $(\mathbf{i}_M, \mathbf{j}_M, \mathbf{k}_M)$,

$$\mathbf{i}_M = \begin{bmatrix} r_{11} \\ r_{21} \\ r_{31} \end{bmatrix}, \quad \mathbf{j}_M = \begin{bmatrix} r_{12} \\ r_{22} \\ r_{32} \end{bmatrix}, \quad \mathbf{k}_M = \begin{bmatrix} r_{13} \\ r_{23} \\ r_{33} \end{bmatrix}. \tag{5}$$

Transformation of $^M\mathbf{P}$ into $^E\mathbf{P}$ contains rotation and translation,

$$^E\mathbf{P} = _M^E\mathbf{R}(\psi_2, \psi_3)^M\mathbf{P} + \mathbf{X}. \tag{6}$$

Let the cylinder rotate around $(\mathbf{i}_M, \mathbf{j}_M, \mathbf{k}_M)$ with angles $(\varphi_1, \varphi_2, \varphi_3)$ (Fig. 2). The angular velocity of cylinder is calculated by

$$\omega_1 = \frac{d\varphi_1}{dt}, \quad \omega_2 = \frac{d\varphi_2}{dt}, \quad \omega_3 = \frac{d\varphi_3}{dt}, \tag{7}$$

and

$$\psi_1 = \varphi_1, \quad \frac{d\psi_2}{dt} = \frac{d\varphi_2}{dt} = \omega_2, \quad \frac{d\psi_3}{dt} \neq \frac{d\varphi_3}{dt}. \quad (8)$$

If $(\omega_1, \omega_2, \omega_3)$ are given, time integration of (7) with the time interval Δt leads to

$$\Delta\varphi_1 = \omega_1 \Delta t, \quad \Delta\varphi_2 = \omega_2 \Delta t, \quad \Delta\varphi_3 = \omega_3 \Delta t. \quad (9)$$

The increments $(\Delta\psi_2, \Delta\psi_3)$ are determined by the relationship between the two rotation matrices $_M^E R(\psi_2 + \Delta\psi_2, \psi_3 + \Delta\psi_3)$ and $_M^E R(\psi_2, \psi_3)$;

$$_M^E R(\psi_2 + \Delta\psi_2, \psi_3 + \Delta\psi_3) = {}_M^E R(\psi_2, \psi_3) \begin{bmatrix} \cos(\Delta\varphi_3) & -\sin(\Delta\varphi_3) & 0 \\ \sin(\Delta\varphi_3) & \cos(\Delta\varphi_3) & 0 \\ 0 & 0 & 1 \end{bmatrix}$$
$$\times \begin{bmatrix} \cos(\Delta\varphi_2) & 0 & \sin(\Delta\varphi_2) \\ 0 & 1 & 0 \\ -\sin(\Delta\varphi_2) & 0 & \cos(\Delta\varphi_2) \end{bmatrix}. \quad (10)$$

2.3 F-Coordinate. The F-coordinate is represented by $F_F(\mathbf{X}, \mathbf{i}_F, \mathbf{j}_F, \mathbf{k}_F)$ with the origin $\mathbf{X}$, unit vectors $(\mathbf{i}_F, \mathbf{j}_F, \mathbf{k}_F)$, and coordinates (x_F, y_F, z_F). Let $\mathbf{V}_w$ be the fluid velocity. The fluid-to-cylinder velocity is represented by $\mathbf{V}_r = \mathbf{V}_w - \mathbf{V}$ that is decomposed into two parts,

$$\mathbf{V}_r = \mathbf{V}_1 + \mathbf{V}_2, \quad \mathbf{V}_1 = V_1 \mathbf{i}_F, \quad \mathbf{V}_2 = V_2 \mathbf{j}_F, \quad (11)$$

where

$$\mathbf{V}_1 = (\mathbf{V}_r \cdot \mathbf{i}_F) \mathbf{i}_F$$

is the component parallel to the cylinder's main axis (i.e., along $\mathbf{i}_M$), and

$$\mathbf{V}_2 = \mathbf{V}_r - (\mathbf{V}_r \cdot \mathbf{i}_F) \mathbf{i}_F$$

is the component perpendicular to the cylinder's main-axial direction. The unit vectors for the F-coordinate are defined by (column vectors)

$$\mathbf{i}_F = \mathbf{i}_M = \begin{bmatrix} r_{11} \\ r_{21} \\ r_{31} \end{bmatrix}, \quad \mathbf{j}_F = \mathbf{V}_2 / |\mathbf{V}_2|, \quad \mathbf{k}_F = \mathbf{i}_F \times \mathbf{j}_F. \quad (12)$$

The F-coordinate system is solely determined by orientation of the cylinder's main-axis ($\mathbf{i}_M$) and the water-to-cylinder velocity. Note that the M- and F-coordinate systems have one common unit vector $\mathbf{i}_M$ (orientation of the cylinder).

Let $_F^E \mathbf{R}$ be the rotation matrix from the F-coordinate to the E-coordinate,

$$_F^E \mathbf{R}(\psi_2, \psi_3, \phi_{MF}) \equiv \begin{bmatrix} r_{11} & r'_{12} & r'_{13} \\ r_{21} & r'_{22} & r'_{23} \\ r_{31} & r'_{32} & r'_{33} \end{bmatrix}, \quad \phi_{MF} \equiv (\mathbf{j}_M, \mathbf{j}_F), \quad (13)$$

which leads to

$$\mathbf{i}_F = \begin{bmatrix} r_{11} \\ r_{21} \\ r_{31} \end{bmatrix}, \quad \mathbf{j}_F = \begin{bmatrix} r'_{12} \\ r'_{22} \\ r'_{32} \end{bmatrix}, \quad \mathbf{k}_F = \begin{bmatrix} r'_{13} \\ r'_{23} \\ r'_{33} \end{bmatrix}. \quad (14)$$

Here, ϕ_{MF} is the angle between the two unit vectors $(\mathbf{j}_M, \mathbf{j}_F)$. Let the vector $\mathbf{P}$ be represented by $^F\mathbf{P}$ in the F-coordinate. Transformation of $^F\mathbf{P}$ into $^E\mathbf{P}$ contains rotation and translation,

$$^E\mathbf{P} = {}_F^E \mathbf{R}(\psi_2, \psi_3, \phi_{MF}) {}^F\mathbf{P} + \mathbf{X}. \quad (15)$$

Use of the F-coordinate system simplifies the calculations for the lift and drag forces and torques acting on the cylinder. Since the M- and F-coordinates share a common axis $\mathbf{i}_M = \mathbf{i}_F$, the rotation matrix from the F- to M- coordinate systems is given by

$$_F^M \mathbf{R} = {}_E^M \mathbf{R} {}_F^E \mathbf{R} = {}_M^E \mathbf{R}^{-1}(\psi_2, \psi_3) {}_F^E \mathbf{R}(\psi_2, \psi_3, \phi_{MF}) = \begin{bmatrix} 1 & 0 & 0 \\ 0 & e_{22} & e_{23} \\ 0 & e_{32} & e_{33} \end{bmatrix}$$
$$(16)$$

it is two-dimensional with the rotation matrix given by

$$_F^M \mathbf{E} = \begin{bmatrix} \mathbf{e}_2 & \mathbf{e}_3 \end{bmatrix}, \quad \mathbf{e}_2 = \begin{bmatrix} e_{22} \\ e_{32} \end{bmatrix}, \quad \mathbf{e}_3 = \begin{bmatrix} e_{23} \\ e_{33} \end{bmatrix}. \quad (17)$$

Let the cylinder rotate around $(\mathbf{i}_F, \mathbf{j}_F, \mathbf{k}_F)$ with the angular velocity components represented by $(\omega_1^F, \omega_2^F, \omega_3^F)$ (Fig. 2). They are connected to the angular velocity components in the M-coordinate system by

$$\omega_1^F = \omega_1, \quad \begin{bmatrix} \omega_2^F \\ \omega_3^F \end{bmatrix} = {}_M^F \mathbf{E} \begin{bmatrix} \omega_2 \\ \omega_3 \end{bmatrix}. \quad (18)$$

3 Dynamics

3.1 Momentum Balance. The translation velocity of the cylinder ($\mathbf{V}$) is governed by the momentum equation in the E-coordinate system,

$$\frac{d}{dt} \begin{bmatrix} u \\ v \\ w \end{bmatrix} = -\begin{bmatrix} 0 \\ 0 \\ g \end{bmatrix} + \frac{\mathbf{F}_{nh} + \mathbf{F}_h}{\rho \Pi}, \quad (19a)$$

where g is the gravitational acceleration, Π is the cylinder volume, ρ is the rigid body density, $\rho\Pi = m$, is the cylinder mass, $\mathbf{F}_{nh}$ is the nonhydrodynamic force, and $\mathbf{F}_h$ is the hydrodynamic force (i.e., surface force including drag, lift, impact forces). Both $\mathbf{F}_{nh}$ and $\mathbf{F}_h$ are integrated for the cylinder. The drag and lift forces are calculated using the drag and lift laws with the given water-to-cylinder velocity ($\mathbf{V}_r$). In the F-coordinate, $\mathbf{V}_r$ is decomposed into along-cylinder ($\mathbf{V}_1$) and across-cylinder ($\mathbf{V}_2$) components.

The nonhydrodynamic force $\mathbf{F}_{nh}$ is the buoyancy force ($\mathbf{F}_b$) for the air and water phases,

$$\mathbf{F}_{nh} = \mathbf{F}_b = \mathbf{k}(\rho_a \Pi g, \rho_w \Pi g),$$

where (ρ_a, ρ_w) are the air and water densities. $\mathbf{F}_{nh}$ is the resultant of the buoyancy force ($\mathbf{F}_b$), pore water pressure force ($\mathbf{F}_{pw}$), and shearing resistance force ($\mathbf{F}_s$) for the sediment phase (see Sec. 6).

3.2 Moment of Momentum Equation. It is convenient to write the moment of momentum equation,

$$\mathbf{J} \cdot \frac{d\boldsymbol{\omega}}{dt} = -2\mathbf{J} \cdot (\boldsymbol{\Omega} \times \boldsymbol{\omega}) + \mathbf{M}_{nh} + \mathbf{M}_h, \quad (20)$$

in the M-coordinate system with the cylinder's angular velocity components $(\omega_1, \omega_2, \omega_3)$ defined by (19a) and (19b). Here, the first term on the right-hand side is an apparent torque (similar to the Corilois term in earth science) due to the use of the rotating coordinate system (i.e., the M-coordinate), and

$$\boldsymbol{\Omega} = \omega_2 \mathbf{j}_M + \omega_3 \mathbf{k}_M \quad (21)$$

is the angular velocity of the M-coordinate system. If $\omega_1 = 0$, then $\boldsymbol{\Omega} = \boldsymbol{\omega}$, which leads to

$$-2\mathbf{J} \cdot (\boldsymbol{\Omega} \times \boldsymbol{\omega}) = \begin{cases} 0, & \text{if } \omega_1 = 0 \ (\text{i.e.,} \boldsymbol{\Omega} = \boldsymbol{\omega}), \\ -2J_2\omega_1\omega_3 \mathbf{j}_M + 2J_3\omega_1\omega_2 \mathbf{k}_M, & \text{if } \omega_1 \neq 0. \end{cases} \quad (22)$$

In this study, the apparent torque is neglected. The gravity force, passing the COM, does not induce the moment. $\mathbf{M}_{nh}$ and $\mathbf{M}_h$ are the nonhydrodynamic and hydrodynamic force torques. In the M-coordinate system, the moment of gyration tensor for the axially symmetric cylinder is a diagonal matrix
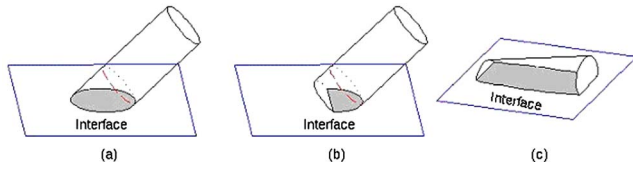
Fig. 3 Three patterns of cylinder penetration with the cross section being (a) a complete ellipse, (b) a cutoff ellipse with one side straight line, and (c) a cutoff ellipse with two side straight lines

$$\mathbf{J} = \begin{bmatrix} J_1 & 0 & 0 \\ 0 & J_2 & 0 \\ 0 & 0 & J_3 \end{bmatrix}, \tag{23}$$

where J_1, J_2, and J_3 are the moments of inertia. The buoyancy force induces the moment in the $\mathbf{j}_M$ direction if the COM does not coincide with the COV (i.e., $\chi \neq 0$),

$$\mathbf{M}_b = |\mathbf{F}_b| \chi \cos \psi_2 \mathbf{j}_M. \tag{24}$$

Computation of nonhydrodynamic and hydrodynamic forces $(\mathbf{F}_{nh}, \mathbf{F}_h)$ and torques $(\mathbf{M}_{nh}, \mathbf{M}_h)$ is more complicated for a cylinder penetrating through air-water and water-sediment interfaces than falling through a single medium such as water. At the instance when the cylinder penetrates into an interface, three situations may exist: the cross section is a complete ellipse [Fig. 3(a)], a cutoff ellipse with one side straight line [Fig. 3(b)], or a cutoff ellipse with two straight lines [Fig. 3(c)]. The interface separates the cylinder to two parts. Each part contains a noncylinder D and a subcylinder C (Fig. 4). Let (L_c, L_d), (Ω_c, Ω_d) and (Π_c, Π_d) be the lengths, surfaces, and volumes of $[C, D]$, and (h_1, h_2) the depths of the two sides of D (Fig. 5). The characteristics of the geometric parameters (L_c, h_1, h_2) are listed in Table 1. The COV for the portion $[C, D]$ is called the partial COV (PCOV).

4 Equivalent Cylinder Method

4.1 Equivalent Cylinder. During penetration, the part that contacts fluid (air or water) is treated as a cylinder [E] with the same mass and PCOV location and with the assumption that the buoyancy and hydrodynamic forces and torques for $[C, D]$ are the same for [E]. The cylinder [E], called the equivalent cylinder, is used to represent the part $[C, D]$. Thus, the theoretical procedure developed for calculating external forcing (buoyancy and hydrodynamic forces and torques) for a cylinder [8] can be easily used for [E].
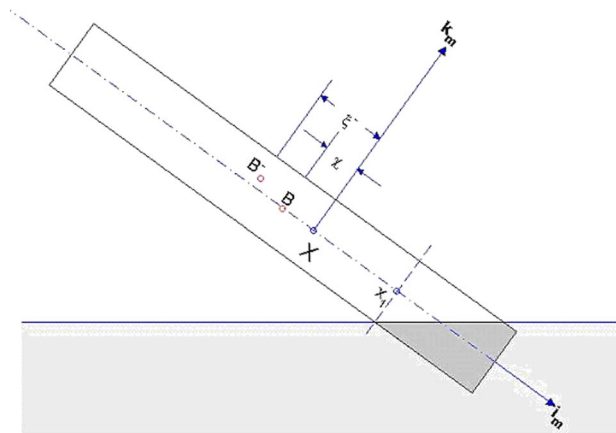

Fig. 4 Illustration of PCOV (B⁻), x_1, and ξ^- for the tail part $[C^{(1)}, D^{(1)}]$ for the case in Fig. 3(a)
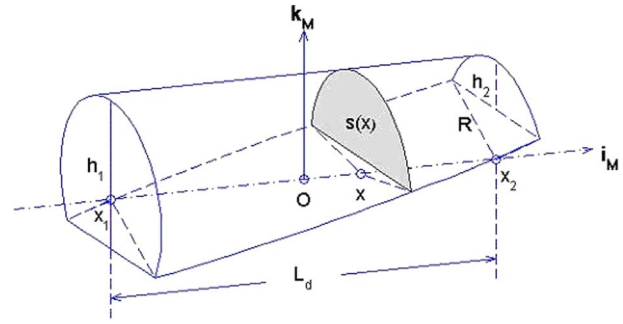

Fig. 5 Geometry of the part $D^{(1)}$

4.2 Volume of $[C, D]$. In the M-coordinate system, the area of the vertical cross section of D is given by

$$s(x) = R^2 \cos^{-1}\left(1 - \frac{h(x)}{R}\right) - [R - h(x)]\sqrt{R^2 - [R - h(x)]^2}, \tag{25a}$$

where $h(x)$ is the depth of the cross section,

$$h(x) = h_1 + \frac{\Delta h}{L_d}(x - x_1), \quad \Delta h = h_2 - h_1, \tag{25b}$$

where L_d is the length of D (see Fig. 5). Integration of $s(x)$ along x axis gives the volume of D,

$$\Pi_d = \int_{x_1}^{x_2} s(x)dx = \frac{R^3 L_d}{\Delta h}\beta(\kappa_1, \kappa_2) = \pi R^2 l_d, \tag{26}$$

where

$$\kappa_1 = 1 - \frac{h_1}{R}, \quad \kappa_2 = 1 - \frac{h_2}{R}, \tag{27a}$$

$$\beta(\kappa_1, \kappa_2) \equiv \kappa_1 \cos^{-1}(\kappa_1) - \sqrt{1 - \kappa_1^2} + \frac{1}{3}(1 - \kappa_1^2)^{3/2} - \kappa_2 \cos^{-1}(\kappa_2)$$
$$+ \sqrt{1 - \kappa_2^2} - \frac{1}{3}(1 - \kappa_2^2)^{3/2}, \tag{27b}$$

and

$$l_d = \frac{R L_d}{\pi \Delta h}\beta(\kappa_1, \kappa_2). \tag{27c}$$

Here, l_d is the equivalent length of D. The volume of C is calculated by

$$\Pi_c = \pi R^2 L_c. \tag{28}$$

The total volume of $[C, D]$ is

$$\Pi = \pi R^2 l,$$

and

$$l = L_c + l_d$$

is the length of the equivalent cylinder E.

Table 1 Geometric parameters during the cylinder penetration

	L_c	h_1	h_2
Upper and lower parts of Fig. 3(a)	>0	2R	0
Upper part of Fig. 3(b)	>0	2R	0~2R
Lower part of Fig. 3(b)	0	0~2R	0
Upper and lower parts of Fig. 3(c)	0	0~2R	0~2R

4.3 PCOV of [C,D]. Let (ξ^+, η^+) and (ξ^-, η^-) be the PCOV of the head $[C,D]$ (in the direction of $\mathbf{i}_M$) or tail (in the opposite direction of $\mathbf{i}_M$) $[C,D]$ (denoted by $B^{\pm}$, positive sign for the head part) in the M-coordinate system,

$$(\xi^{\pm}, \eta^{\pm}) = \frac{1}{\Pi}\left[\iiint_{\Pi_c}(x,z)dv + \iiint_{\Pi_d}(x,z)dv\right]$$

$$= \frac{1}{\Pi_c + \Pi_d}\left[\left(x_1 \pm \frac{L_c}{2}, 0\right)\Pi_c + \int_{x_1}^{x_2}(x,z)s(x)dx\right].$$

$$(29)$$

where x_1 is defined as the location of interface between C and D. Substitution of (25a), (25b), (26), and (28) into (29) leads to

$$\xi^{\pm} = x_1 \mp \frac{R\Delta h}{\beta(\kappa_1, \kappa_2)L_d(1 + \pi\Delta h L_c\beta^{-1}L_d^{-1})}$$

$$\times\left[\left(\frac{L_d}{\Delta h}\right)^2\mu_x(\kappa_1, \kappa_2) \pm \frac{1}{2}\left(\frac{L_c}{R}\right)^2\right],$$

$$(30)$$

$$\eta^{\pm} = \pm\,\text{sign}(\cos\Psi_2)\frac{R}{6\beta(\kappa_1, \kappa_2)(1 + \pi\Delta h L_c\beta^{-1}L_d^{-1})}\mu_z(\kappa_1, \kappa_2),$$

$$(31)$$

where

$$\mu_x(\kappa_1, \kappa_2) \equiv \frac{1}{4}\Big[(2\kappa_2^2 - 1)\cos^{-1}\kappa_2 - (2\kappa_1^2 - 1)\cos^{-1}\kappa_1 + \kappa_1\sqrt{1 - \kappa_1^2}$$

$$-\kappa_2\sqrt{1 - \kappa_2^2}\Big] + \frac{1}{4}\Big[\kappa_2\sqrt{(1 - \kappa_2^2)^3} - \kappa_1\sqrt{(1 - \kappa_1^2)^3}\Big]$$

$$-\frac{1}{8}(\kappa_2\sqrt{1 - \kappa_2^2} - \kappa_1\sqrt{1 - \kappa_1^2} + \sin^{-1}\kappa_2 - \sin^{-1}\kappa_1)$$

$$-\kappa_1(\kappa_2\cos^{-1}\kappa_2 - \kappa_1\cos^{-1}\kappa_1 + \sqrt{1 - \kappa_1^2} - \sqrt{1 - \kappa_2^2})$$

$$-\frac{\kappa_1}{3}\Big[\sqrt{(1 - \kappa_2^2)^3} - \sqrt{(1 - \kappa_1^2)^3}\Big],$$

$$\mu_z(\kappa_1, \kappa_2) \equiv \kappa_1\sqrt{(1 - \kappa_1^2)^3} - \kappa_2\sqrt{(1 - \kappa_2^2)^3} + \frac{3}{2}\Big(\kappa_1\sqrt{1 - \kappa_1^2}$$

$$-\kappa_2\sqrt{1 - \kappa_2^2} + \sin^{-1}\kappa_1 - \sin^{-1}\kappa_2\Big).$$

$$(32)$$

Let (ξ, η) be (ξ^+, η^+) for the head part and (ξ^-, η^-) for the tail part. The position vector of PCOV in the M-coordinate system is represented by

$$\mathbf{r}_{\text{PCOV}} = \xi\mathbf{i}_M + \eta\mathbf{k}_M.$$

$$(33)$$

5 Forces and Torques in Air and Water

Calculation of the buoyancy force and torque is straightforward. Calculation of the surface force and torque is not simple. Assume that the surface force and torque on the equivalent cylinder E are the same on the $[C,D]$. If $[C,D]$ moves in fluid (air or water), the recursive model recently developed [8] can be used to calculate for equivalent cylinder E. Thus, the water column is taken as the example to illustrate the calculation of the hydrodynamic force and torque. Computation of the surface force and torque due to sediment is described in Sec. 6.

5.1 Buoyancy Force and Torque. The buoyancy force $\mathbf{F}_b$ is the product of the air (or water) density and volume,

$$\mathbf{F}_b = \rho(\Pi_c + \Pi_d)\mathbf{k} = \rho\pi R^2(L_c + l_d)\mathbf{k}.$$

$$(34)$$

The torque due to the buoyancy force for the upper or lower part is given by

$$\mathbf{M}_b = \mathbf{r}_{\text{PCOV}} \times \mathbf{F}_b.$$

$$(35)$$

Substitution of (33) and (34) into (35) leads to

$$\mathbf{M}_b = -\rho\pi R^2(L_c + l_d)(\xi\cos\psi_2 + \eta\sin\psi_2)\mathbf{j}_M.$$

$$(36)$$

5.2 Drag and Lift Forces. The drag and lift forces exerted on the cylinder is represented by

$$\mathbf{F}_h = (F_{d1}\mathbf{i}_F + F_{d2}\mathbf{j}_F + F_{d3}\mathbf{k}_F) + \mathbf{F}_l,$$

$$(37)$$

where (F_{d1}, F_{d2}, F_{d3}) are the components of drag force along $\mathbf{i}_F$ (along-cylinder), $\mathbf{j}_F$ (across-cylinder) and $\mathbf{k}_F$ directions. $\mathbf{F}_l$ represented the lift force. Linearization of drag and lift laws is used in the computation.

Let (C_{d1}, C_{d2}) be the drag coefficients in the along- and across-cylinder directions (Reynolds number dependent). The drag force coefficients are calculated on the base of steady flow; they is different from the fluid around an accelerated solid body. The added mass correction is represented by the ratios (f_1, f_2, f_3) in the three directions of the F-coordinate system.

The drag force along $\mathbf{i}_F$ is calculated by

$$F_{d1} = C_{td1}(t)V_1,$$

$$(38)$$

$$C_{td1}(t) \equiv C_{d1}\frac{\pi R^2}{2}\frac{\rho_w}{(1 + f_1)}|V_1(t)|.$$

$$(39)$$

C_{d1} is almost independent on the axial Reynolds number (Re) when $\text{Re} > 10^4$, but dependent on the cylinder's aspect ratio [9],

$$C_{d1} = \begin{cases} 1.0, & \text{if } \delta > 8, \\ 0.75 + \delta/32.1934 + 0.09612/\delta^2, & \text{if } 8 \geqslant \delta > 0.5, \\ 1.15, & \text{if } \delta \leqslant 0.5. \end{cases}$$

$$(40)$$

Substitution of (11) and (12) into (38) leads to

$$F_{d1}\mathbf{i}_F = -C_{td1}(t)\mathbf{I}_{11}\cdot\left(\begin{bmatrix} u \\ v \\ w \end{bmatrix} - \begin{bmatrix} u_w \\ v_w \\ w_w \end{bmatrix}\right), \quad \mathbf{I}_{11} = \mathbf{i}_F\mathbf{i}_F^T,$$

$$(41)$$

where the superscript "T" denotes the transpose.

The drag force along $\mathbf{j}_F$ is calculated by

$$F_{d2} = R\int_{-L/2-\chi}^{L/2-\chi}C_{d2}(V_2')^2\frac{\rho_w}{(1 + f_2)}d\eta = C_{td2}(t)V_2 + f_{rd2}(t),$$

$$(42)$$

where

$$V_2'(\eta) = V_2 - \omega_3^F\eta$$

is the water-to-cylinder velocity at the surface in the $\mathbf{j}_F$ direction and

$$C_{td2}(t) \equiv 2C_{d2}LR\frac{\rho_w}{(1 + f_2)}\left(\frac{V_2}{2} + \chi\omega_3^F\right),$$

$$(43a)$$

$$f_{rd2}(t) \equiv 2C_{d2}LR\frac{\rho_w}{(1 + f_2)}\left(\frac{1}{2}\chi^2 + \frac{1}{24}L^2\right)(\omega_3^F)^2.$$

$$(43b)$$

An empirical formula is used for calculating C_{d2} [10]

$$C_{d2} = \begin{cases} 1.9276 + 8/\text{Re}, & \text{if } \text{Re} \leq 12, \\ 1.261 + 16/\text{Re}, & \text{if } 12 < \text{Re} \leq 180, \\ 0.855 + 89/\text{Re}, & \text{if } 180 < \text{Re} \leq 2000, \\ 0.84 + 0.000\,03\,\text{Re}, & \text{if } 2000 < \text{Re} \leq 12{,}000, \\ 1.2 - 4/\delta, & \text{if } 12{,}000 < \text{Re} \leq 150{,}000, \quad \delta \geq 10, \\ 0.835 - 0.35/\delta, & \text{if } 12{,}000 < \text{Re} \leq 150{,}000, \quad 2 \leq \delta < 10, \\ 0.7 - 0.08/\delta, & \text{if } 12{,}000 < \text{Re} \leq 150{,}000, \quad \delta < 2, \\ 1.875 - 0.000\,004\,5\,\text{Re}, & \text{if } 150{,}000 < \text{Re} \leq 350{,}000, \\ 1/(641{,}550/\text{Re} + 1.5), & \text{if } \text{Re} > 350{,}000. \end{cases} \quad (44)$$

Substitution of (11) and (12) into (42) leads to

$$F_{d2}\mathbf{j}_\text{F} = - C_{td2}(t)\mathbf{I}_{22} \cdot \left(\begin{bmatrix} u \\ v \\ w \end{bmatrix} - \begin{bmatrix} u_w \\ v_w \\ w_w \end{bmatrix} \right) + f_{rd2}(t)\mathbf{j}_\text{F}, \quad \mathbf{I}_{22} = \mathbf{j}_\text{F}\mathbf{j}_\text{F}^\text{T}. \quad (45)$$

The angular velocity (ω_2^F) causes nonuniform water-to-cylinder velocity in the $\mathbf{k}_\text{F}$ direction,

$$V_3 = \omega_2^F \eta. \quad (46)$$

The drag force along $\mathbf{k}_\text{F}$ is calculated by

$$\mathbf{F}_{d3} = \left[C_{d2}R\frac{\rho_w}{(1+f_2)}\omega_2^F|\omega_2^F|\left(\int_0^{\frac{L}{2}-\chi} \eta^2 d\eta - \int_{-\frac{L}{2}-\chi}^0 \eta^2 d\eta \right) \right]\mathbf{k}_\text{F}$$
$$= f_{rd3}(t)\mathbf{k}_F, \quad (47)$$

where

$$f_{rd3}(t) \equiv -\frac{1}{6}C_{d2}\frac{\rho_w R}{(1+f_2)}\chi(3L^2 + 4\chi^2)|\omega_2^F|\omega_2^F \quad (48)$$

is the rotational drag force in the $\mathbf{k}_\text{F}$ direction.

The water-to-cylinder velocity determines the lift force [11]

$$\mathbf{F}_l = \left[\frac{C_{tl}(t)}{L}\int_{-L/2-\chi}^{L/2-\chi} V_2'(\eta)d\eta \right]\mathbf{k}_\text{F}, \quad C_{tl}(t) \equiv C_l L R\frac{\rho_w}{(1+f_2)}|V_2|, \quad (49)$$

where C_l is the lift coefficient. An empirical formula is used for calculating C_l [12],

$$C_l = \begin{cases} 2\omega_1 R/V_2, & \text{if } \omega_1 R/V_2 \leq 4, \\ 8 + 0.24(\omega_1 R/V_2 - 4), & \text{if } \omega_1 R/V_2 > 4. \end{cases} \quad (50)$$

Substitution of (11) and (12) into (49) leads to

$$\mathbf{F}_l = - C_{tl}(t)\mathbf{I}_{32} \cdot \left(\begin{bmatrix} u \\ v \\ w \end{bmatrix} - \begin{bmatrix} u_w \\ v_w \\ w_w \end{bmatrix} \right) + f_{rl}(t)\mathbf{k}_\text{F}, \quad \mathbf{I}_{32} = \mathbf{k}_\text{F}\mathbf{j}_\text{F}^\text{T}, \quad (51)$$

where

$$f_{rl}(t) \equiv C_{tl}(t)\chi\omega_3^F$$

is the rotational lift force. Substitution of (41), (45), (47), and (51) into (37) and use of (14) lead to

Journal of Applied Mechanics

$$\mathbf{F}_h = - [C_{td1}(t)\mathbf{I}_{11} + C_{td2}(t)\mathbf{I}_{22} + C_{tl}(t)\mathbf{I}_{32}] \cdot \left(\begin{bmatrix} u \\ v \\ w \end{bmatrix} - \begin{bmatrix} u_w \\ v_w \\ w_w \end{bmatrix} \right) + f_{rd2}(t)$$
$$\times \begin{bmatrix} r_{12}' \\ r_{22}' \\ r_{32}' \end{bmatrix} + [f_{rd3}(t) + f_{rl}(t)]\begin{bmatrix} r_{13}' \\ r_{23}' \\ r_{33}' \end{bmatrix}. \quad (52)$$

Substitution of (52) into (19a) leads to the cylinder's momentum equation,

$$\frac{d}{dt}\begin{bmatrix} u \\ v \\ w \end{bmatrix} = - \mathbf{D} \cdot \begin{bmatrix} u \\ v \\ w \end{bmatrix} + \boldsymbol{\alpha}_1, \quad (19b)$$

where

$$\boldsymbol{\alpha}_1 \equiv \mathbf{D} \cdot \begin{bmatrix} u_w \\ v_w \\ w_w \end{bmatrix} - \begin{bmatrix} 0 \\ 0 \\ (1 - \rho_w/\rho)g \end{bmatrix} + b_1\begin{bmatrix} r_{12}' \\ r_{22}' \\ r_{32}' \end{bmatrix} + b_2\begin{bmatrix} r_{13}' \\ r_{23}' \\ r_{33}' \end{bmatrix},$$

$$\mathbf{D} \equiv \frac{C_{td1}(t)\mathbf{I}_{11} + C_{td2}(t)\mathbf{I}_{22} + C_{tl}(t)\mathbf{I}_{23}}{\rho\Pi}, \quad b_1 \equiv \frac{f_{rd2}(t)}{\rho\Pi},$$

$$b_2 \equiv \frac{f_{rd3}(t) + f_{rl}(t)}{\rho\Pi}.$$

5.3 Drag and Lift Torques. For an axially symmetric cylinder, the moment of the hydrodynamic force in the $\mathbf{i}_\text{F}$ direction is not caused by the drag and lift forces, but by the viscous fluid. The moment of the viscous force of steady flow between two rotating cylinders with the common axis is calculated by [1]

$$M = 4\pi\mu\frac{r_1^2 \cdot r_0^2}{r_1^2 - r_0^2}(\omega_1 - \omega_0),$$

where (r_1, r_0) and (ω_1, ω_0) are the radii and angle velocities of the inner and outer cylinders and μ is the viscosity. The moment of the viscous force on one rotating cylinder is th limit case of the two rotating cylinders as $r_0 \to \infty$ and $\omega_0 = 0$. The moment of the viscous force around $\mathbf{i}_\text{F}$ is calculated by

$$\mathbf{M}_{v1} = - C_{m1}\omega_1\mathbf{i}_\text{F}, \quad C_{m1} \equiv \pi\mu L d^2. \quad (53)$$

Same as the hydrodynamic forces, the torques along the $\mathbf{j}_\text{F}$ and $\mathbf{k}_\text{F}$ axes, $(\mathbf{M}_{d1}, \mathbf{M}_{d2}, \mathbf{M}_l)$, are calculated. When the cylinder rotates around $\mathbf{j}_\text{F}$ with the angular velocity ω_2^F, the drag force causes a torque on the cylinder in the $\mathbf{j}_\text{F}$ direction,

$$\mathbf{M}_{d2} = \left[-\omega_2^F|\omega_2^F|\int_{-L/2-\chi}^{L/2-\chi} C_{d2}R\frac{\rho_w}{(1+f_r)}\eta^2|\eta|d\eta \right]\mathbf{j}_\text{F}$$
$$= - [C_{m2}(t)\omega_2^F]\mathbf{j}_\text{F}, \quad (54)$$

$$C_{m2}(t) \equiv \frac{1}{2} C_{d2} R \frac{\rho_w}{(1+f_r)} \left(\frac{1}{16} L^4 + \frac{3}{2} L^2 \chi^2 + \chi^4 \right) |\omega_2^F|,$$

where f_r is the added mass factor for the moment of drag and lift forces. If the water-to-cylinder velocity or the cylinder mass distribution is nonuniform ($\chi \neq 0$), the drag force causes a torque on the cylinder in the $\mathbf{k}_F$ direction,

$$\mathbf{M}_{d3} = \left[\int_{-L/2-\chi}^{L/2-\chi} C_{d2} R \frac{\rho_w}{(1+f_r)} (V_2 - \omega_3^F \eta)^2 \eta d\eta \right] \mathbf{k}_F$$
$$= -[C_{m3}(t)\omega_3^F + M_3(t)]\mathbf{k}_F, \qquad (55)$$

$$C_{m3}(t) \equiv C_{d2} R \frac{\rho_w}{(1+f_r)} \left(\frac{1}{6} V_2 L^3 + V_2 L\chi^2 + \frac{1}{4} L^3 \omega_3^F \chi + L\chi^3 \omega_3^F \right), \qquad (56a)$$

$$M_3(t) \equiv C_{d2} R \frac{\rho_w}{(1+f_r)} V_2^2 L\chi. \qquad (56b)$$

The lift force exerts a torque on the cylinder in the $\mathbf{j}_F$ direction,

$$\mathbf{M}_{l2} = \left[-\int_{-L/2-\chi}^{L/2-\chi} C_l R \frac{\rho_w}{f_{kr}} (V_2 - \omega_3^F \eta) \eta d\eta \right] \mathbf{j}_F$$
$$= [C_{ml}(t)\omega_3^F + M_l(t)]\mathbf{j}_F, \qquad (57)$$

$$C_{ml}(t) \equiv C_l V_2 R \frac{\rho_w}{(1+f_r)} L \left(\frac{1}{12} L^2 + \chi^2 \right), \quad M_l(t) \equiv R \frac{\rho_w}{f_{kr}} L V_2^2 \chi. \qquad (58)$$

After the angular velocity components (ω_2^F, ω_3^F) are transformed into (ω_2, ω_3) (from the F-coordinate to the M-coordinate) using (18), and the unit vectors ($\mathbf{j}_F, \mathbf{k}_F$) are transformed into ($\mathbf{j}_M, \mathbf{k}_M$) using the rotation matrix (17), the drag force torques in the $\mathbf{j}_F$ direction (54) and in the $\mathbf{k}_F$ direction (55) are represented by

$$\mathbf{M}_{d2} = -C_{m2}(t)\mathbf{H}_{22} \cdot \begin{bmatrix} \omega_2 \\ \omega_3 \end{bmatrix}, \quad \mathbf{H}_{22} = \mathbf{e}_2 \mathbf{e}_2^T, \qquad (59)$$

$$\mathbf{M}_{d3} = -C_{m3}(t)\mathbf{H}_{33} \cdot \begin{bmatrix} \omega_2 \\ \omega_3 \end{bmatrix} - M_3(t)\mathbf{e}_3, \quad \mathbf{H}_{33} = \mathbf{e}_3 \mathbf{e}_3^T, \qquad (60)$$

and the lift torque in the $\mathbf{j}_F$ (57) is represented by

$$\mathbf{M}_{l2} = C_{ml}(t)\mathbf{H}_{23} \cdot \begin{bmatrix} \omega_2 \\ \omega_3 \end{bmatrix} + M_l(t)\mathbf{e}_2, \quad \mathbf{H}_{23} = \mathbf{e}_2 \mathbf{e}_3^T. \qquad (61)$$

Summation of (53) and (59)–(61) leads to

$$\mathbf{M}_h = \mathbf{M}_\nu + \mathbf{M}_{d2} + \mathbf{M}_{d3} + \mathbf{M}_{l2}$$
$$= -C_{m1}\omega_1 \mathbf{i}_F - [C_{m2}(t)\mathbf{H}_{22} + C_{m3}(t)\mathbf{H}_{33} - C_{ml}(t)\mathbf{H}_{23}] \cdot \begin{bmatrix} \omega_2 \\ \omega_1 \end{bmatrix}$$
$$+ M_l(t)\mathbf{e}_2 - M_3(t)\mathbf{e}_3. \qquad (62)$$

6 Resistant Forces in Sediment

6.1 Water Cavity. As the cylinder impacts and penetrates into the sediment, it pushes the sediment and leaves space in the wake. This space is refilled by water right away and a water cavity is produced (Fig. 6). At the instant of the penetration, the total resistant force on the cylinder is represented by

$$\mathbf{F}^s = \int_{\sigma_{sed}} [\delta(\mathbf{f}_b^s + \mathbf{f}_{sh}) + \mathbf{f}_b^w + \mathbf{f}_h^w]d\sigma + \mathbf{F}_{pw}, \qquad (63)$$

where ($\mathbf{f}_b^s, \mathbf{f}_{sh}$) and ($\mathbf{f}_b^w, \mathbf{f}_h^w$) are the sediment buoyancy and shear resistance forces and water buoyancy and hydrodynamic forces
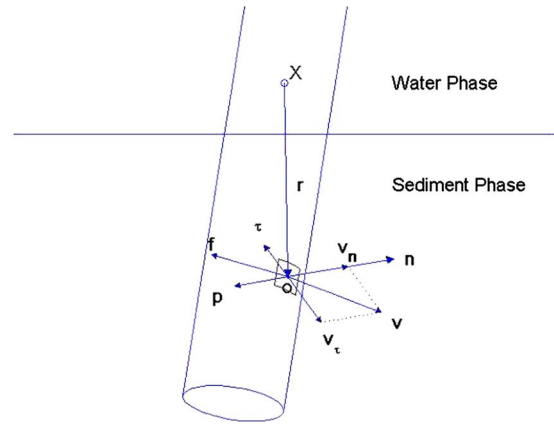

Fig. 6 The impact (resistant) force exerted on the part of the object's surface moving towards the sediment

(per unit area) at the point $\mathbf{r}$ over the cylinder's surface; σ_{sed} is the area of the cylinder's surface below the water-sediment interface; and $\mathbf{F}_{pw}$ is the pore water pressure force on the whole cylinder. In the sediment, the magnitude of the sediment nonhydrostatic force is much larger than the magnitude of the water hydrodynamic force,

$$|\mathbf{f}^s| \gg |\mathbf{f}_h^w|,$$

which means that $\mathbf{f}_h^w$ in (63) can be neglected. The water buoyancy force per unit area over the cylinder's surface is defined by

$$\mathbf{f}_b^w = -\rho_w g(z_{ws} - z)\mathbf{n}, \qquad (64)$$

where z_{ws} is the depth of the water-sediment interface and $\mathbf{n}$ is the unit vector normal to the cylinder surface (outward positive).

Let $\mathbf{v}$ be the velocity at point $\mathbf{r}$ (represented in the M-coordinate) on the cylinder surface,

$$\mathbf{v} = \mathbf{V} + \boldsymbol{\omega} \times \mathbf{r}.$$

The step function δ is defined by

$$\delta = \begin{cases} 1, & \mathbf{v} \cdot \mathbf{n} \geq 0, \\ 0, & \mathbf{v} \cdot \mathbf{n} \leq 0, \end{cases} \qquad (65)$$

which shows that the sediment buoyancy and shear resistance forces act when the cylinder moves towards it. Let $\mathbf{v}_n$ be the normal velocity. The tangential velocity is represented by

$$\mathbf{v}_\tau = \mathbf{v} - \mathbf{v}_n. \qquad (66)$$

The tangential unit vector ($\boldsymbol{\tau}$) is defined by

$$\boldsymbol{\tau} = -\frac{\mathbf{v}_\tau}{|\mathbf{v}_\tau|}, \qquad (67)$$

which is opposite to $\mathbf{v}_\tau$ (Fig. 7).

6.2 Sediment Resistant Forces. When the cylinder impacts and penetrates into the sediment, it will create a large transient pore pressure in the sediment that causes ruptures in the sediment which influences the lifting forces on the cylinder [13,14].

The sediment buoyancy force per unit area is defined by

$$\mathbf{f}_b^s = -\mathbf{n} \int_z^{z_{ws}} \rho_s(z')g dz', \qquad (68)$$

where $\rho_s(z)$ is the sediment density.

The shear resistant force per unit area $\mathbf{f}_{sh}$ depends on the cylinder's penetration speed (V) and the sediment strength. Let $S(z)$ be the sediment shear strength. The shear strength is defined as the maximum stress that a material can withstand before failure in
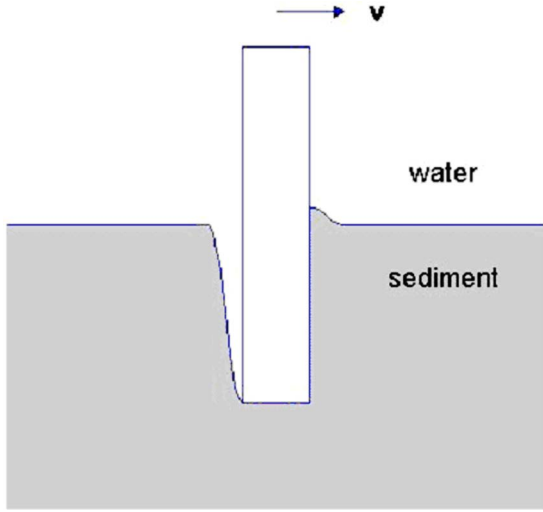
Fig. 7 Momentum and angular momentum balance for the cylinder's penetration through the water-sediment interface

shear. Calculation of shear strength depends upon the test method.

After entering the water-sediment interface, the cylinder reduces its speed (V), and the sediment shearing resistant force also decreases. When the cylinder ceases, the shearing resistant force should be the same as the sediment shear strength $S(z)$. Thus, the shearing resistant force is represented by

$$\mathbf{f}_{sh} = S(z)G(V)\boldsymbol{\tau}, \quad G(0) = 1, \tag{69}$$

where $G(V)$ is the impact function defined by

$$G(V) = A\left[1 - (1 - A^{-1})\exp\left(-\frac{V}{V_{\text{rest}}}\right)\right]. \tag{70}$$

Here, V_{rest} is an infinitesimally small value for V representing the cease of the cylinder in the sediment. The impact function has the following feature,

$$\lim_{V \to \infty} G(V) = A, \tag{71}$$

which shows that when the cylinder impacts on the sediment (usually with large penetration speed), the impact function takes the value of A. Thus, we may call A the impact factor. Note that A and V_{rest} are the two tuning parameters of the numerical model. In this study we use

$$A = 10, \quad V_{\text{rest}} = 0.04 \text{ m s}^{-1}. \tag{72}$$

The shear strength of the sediment is directly measured from the gravity cores using the fall cone apparatus (model G-200) (see Sec. 8.2).

The total force due to the pore water pressure on the cylinder is computed by [15]

$$\mathbf{F}_{pw} = \left[\frac{\pi}{8}\rho_s(z)\left(\frac{gw}{k_p} + \frac{1 + e_v}{e_v}\frac{dw}{dt}\right)B^3\right]\mathbf{k}, \tag{73}$$

where k_p is the permeability coefficient (10^{-4} m s^{-1} [15]), $e_v(\sim 0.50)$ is the void ratio, and B is the length of the rupture line. Substitution of (64), (68), (69), and (73) into (63) leads to

$$\mathbf{F}^s = \int_{\sigma_{\text{sed}}} \boldsymbol{\tau}[\delta\mu G(V)S(z)]d\sigma - \int_{\sigma_{\text{sed}}} \mathbf{n}\left[\left(\delta\int_z^{z_{ws}}\rho_s(z')gdz'\right)\right.$$
$$\left. + \rho_w g(z_{ws} - z)\right]d\sigma + \mathbf{k}\frac{\pi}{8}\rho_s(z)\left(\frac{gw}{k_p} + \frac{1 + e_v}{e_v}\frac{dw}{dt}\right)B^3, \tag{74}$$

which is the external force acted on the cylinder in the sediment phase. The torque due to the sediment ($\mathbf{M}^s$) is calculated by

$$\mathbf{M}^s = \int_{\sigma_{\text{sed}}} (\mathbf{r} \times \boldsymbol{\tau})[\delta\mu G(V)S(z)]d\sigma + \int_{\sigma_{\text{sed}}} (\mathbf{r} \times \mathbf{n})$$
$$\times\left[\left(\delta\int_z^{z_{ws}}\rho_s(z')gdz'\right) + \rho_w g(z_{ws} - z)\right]d\sigma$$
$$+ (\mathbf{r}_{pw} \times \mathbf{k})\frac{\pi}{8}\rho_s(z)\left(\frac{gw}{k} + \frac{1 + e_v}{e_v}\frac{dw}{dt}\right)B^3. \tag{75}$$

where $\mathbf{r}_{pw}$ is the position vector (in the M-coordinate) indicating the location of the cylinder's rupture line.

7 Model Integration

The momentum equation (19a) and (19b) and moment of momentum equation (20) are integrated numerically using the triple coordinate transformation. The momentum equation is integrated in the E-coordinate system. The hydrodynamic (drag and lift) force is transformed from the F-coordinate to the E-coordinate. The moment of momentum equation is integrated in the M-coordinate system. The hydrodynamic torque is transformed from the F-coordinate to the M-coordinate. After the cylinder penetrates into the sediment, the resistant force due to sediment $\mathbf{f}^s$ reduces the cylinder's speed and changes the turning angle.

7.1 Cylinder's Angular Velocity. Substitution of (24) and (62) into (20) leads to the equations for $(\omega_1, \omega_2, \omega_3)$,

$$\frac{d\omega_1}{dt} = -a_1\omega_1, \tag{76}$$

$$\frac{d}{dt}\begin{bmatrix}\omega_2 \\ \omega_3\end{bmatrix} = -\mathbf{B} \cdot \begin{bmatrix}\omega_2 \\ \omega_3\end{bmatrix} + \boldsymbol{\alpha}_2, \tag{77}$$

where

$$a_1 \equiv \frac{C_{m1}}{J_1} = \frac{8\pi\mu L}{\rho\Pi},$$

$$\mathbf{B} \equiv \begin{bmatrix}\frac{1}{J_2} & 0 \\ 0 & \frac{1}{J_3}\end{bmatrix} \cdot [C_{m2}(t)\mathbf{H}_{22} + C_{m3}(t)\mathbf{H}_{33} - C_{ml}(t)\mathbf{H}_{23}],$$

$$\boldsymbol{\alpha}_2 \equiv \begin{bmatrix}\frac{1}{J_2} & 0 \\ 0 & \frac{1}{J_3}\end{bmatrix} \cdot (M_l\mathbf{e}_2 - M_3\mathbf{e}_3) + \frac{\Pi\chi g\rho_w}{J_2}\cos\psi_2\begin{bmatrix}1 \\ 0\end{bmatrix}. \tag{78}$$

Equation (76) has the analytical solution

$$\omega_1(t) = \omega_1(t_0)\exp[-a_1(t - t_0)], \tag{79}$$

which represents damping rotation of the cylinder around the main axis ($\mathbf{i}_M$). Substitution of (79) into (8) leads to

$$\frac{d\varphi_1}{dt} = \omega_1(t_0)\exp[-a_1(t - t_0)],$$

and its integration leads to

$$\varphi_1(t) = -\frac{\omega_1(t_0)}{a_1}\exp[-a_1(t - t_0)] + \varphi_1(t_0). \tag{80}$$

Equations (79) and (80) are the analytic formulas for predicting the angle and angular velocity around the cylinder's main axis (ω_1, φ_1).

7.2 Recursive Procedure. The basic equations (19a), (19b), (77), (79), and (80) describe the dynamics of the falling cylinder. It is noted that the coefficient matrices $\mathbf{B}$, $\mathbf{D}$ and the vectors $\boldsymbol{\alpha}_1$,

α_2 depend on drag/lift coefficients. Besides, $\mathbf{B}$, $\mathbf{D}$, $\boldsymbol{\alpha}_1$, $\boldsymbol{\alpha}_2$ depend on the fluid-to-cylinder velocity and cylinder's angular velocity. Equations (19a), (19b), and (79) are nonlinear equations.

Let matrices $\mathbf{B}$ and $\mathbf{D}$ be separated into diagonal and nondiagonal parts,

$$\mathbf{D} = \mathbf{D}_1 + \mathbf{D}_2, \quad \mathbf{D}_1 \equiv \begin{bmatrix} d_1 & 0 & 0 \\ 0 & d_2 & 0 \\ 0 & 0 & d_3 \end{bmatrix}, \quad \mathbf{D}_2 \equiv \begin{bmatrix} 0 & d_{12} & d_{13} \\ d_{21} & 0 & d_{23} \\ d_{31} & d_{32} & 0 \end{bmatrix},$$
(81)

$$\mathbf{B} = \mathbf{B}_1 + \mathbf{B}_2, \quad \mathbf{B}_1 \equiv \begin{bmatrix} b_1 & 0 \\ 0 & b_2 \end{bmatrix}, \quad \mathbf{B}_2 \equiv \begin{bmatrix} 0 & b_{12} \\ b_{21} & 0 \end{bmatrix}. \quad (82)$$

Substitution of (81) into (19a) and (19b) leads to

$$\frac{d\mathbf{V}}{dt} = -\mathbf{D}_1 \cdot \mathbf{V} + \boldsymbol{\beta}, \quad \boldsymbol{\beta} \equiv \boldsymbol{\alpha}_1 - \mathbf{D}_2 \cdot \mathbf{V}, \quad \mathbf{V} = \begin{bmatrix} u \\ v \\ w \end{bmatrix} \equiv \begin{bmatrix} v_1 \\ v_2 \\ v_3 \end{bmatrix},$$
(83a)

and substitution of (82) into (77) leads to

$$\frac{d}{dt}\begin{bmatrix} \omega_2 \\ \omega_3 \end{bmatrix} = -\mathbf{B}_1 \cdot \begin{bmatrix} \omega_2 \\ \omega_3 \end{bmatrix} + \boldsymbol{\gamma}, \quad \boldsymbol{\gamma} \equiv \boldsymbol{\alpha}_2 - \mathbf{B}_2 \cdot \begin{bmatrix} \omega_2 \\ \omega_3 \end{bmatrix}. \quad (83b)$$

If $\mathbf{B}_1$, $\mathbf{D}_1$, $\boldsymbol{\beta}$, $\boldsymbol{\gamma}$ are taken the values given at the present time step t_n, (83a) and (83b) can be treated as "linear" equations (local linearization) on $[t_n, t_n + \Delta t]$ and integrated analytically,

$$v_i(t_{n+1}) = \begin{cases} v_i(t_n) + \beta_i(t_n)\Delta t, & \text{if } d_i(t_n) = 0, \\ \left(v_i(t_n) - \dfrac{\beta_i(t_n)}{d_i(t_n)} \right)\exp[-d_i(t_n)\Delta t] + \dfrac{\beta_i(t_n)}{d_i(t_n)}, & \text{if } d_i(t_n) \neq 0, \quad i = 1,2,3, \end{cases}$$
(84)

and

$$\omega_i(t_{n+1}) = \begin{cases} \omega_i(t_n) + \gamma_i(t_n)\Delta t, & \text{if } d_i(t_n) = 0, \\ \left(\omega_i(t_n) - \dfrac{\gamma_i(t_n)}{b_i(t_n)} \right)\exp[-b_i(t_n)\Delta t] + \dfrac{\gamma_i(t_n)}{b_i(t_n)}, & \text{if } d_i(t_n) \neq 0, \quad i = 2,3. \end{cases}$$
(85)

Integration of (83a) twice from t_n leads to the translation position of the cylinder at t_{n+1},

$$x_i(t_{n+1}) = \begin{cases} x_i(t_n) + v_i(t_n)\Delta t + \frac{1}{2}\beta_i(t_n)\Delta t^2, & \text{if } d_i(t_n) = 0, \\ x_i(t_n) + \dfrac{\beta_i(t_n)}{d_i(t_n)}\Delta t - \dfrac{1}{d_i(t_n)}\left(v_i(t_n) - \dfrac{\beta_i(t_n)}{d_i(t_n)} \right)\{\exp[-d_i(t_n)\Delta t] - 1\}, & \text{if } d_i(t_n) \neq 0, \end{cases}$$
(86)

where $x_1 \equiv x$, $x_2 \equiv y$, and $x_3 \equiv z$. Integration of (83b) twice from t_n leads to the change of rotation angles (φ_2, φ_3) at t_{n+1},

$$\Delta\varphi_i(t_{n+1}) = \begin{cases} \omega_i(t_n)\Delta t + \frac{1}{2}\gamma_i(t_n)\Delta t^2, & \text{if } b_i(t_n) = 0, \\ \dfrac{\omega_i(t_n)}{b_i(t_n)}\Delta t - \dfrac{1}{b_i(t_n)}\left(\varphi_i(t_n) - \dfrac{\omega_i(t_n)}{b_i(t_n)} \right)\{\exp[-b_i(t_n)\Delta t] - 1\}, & \text{if } b_i(t_n) \neq 0, \quad i = 2,3. \end{cases}$$
(87)

Equations (84) and (85) are the recursive formulas for predicting the cylinder's translation velocity (u,v,w) and angular velocity $(\omega_1, \omega_2, \omega_3)$, and Eqs. (86) and (87) are the recursive formulas for predicting the cylinder's translation position (x,y,z) and rotation angle increments $(\Delta\varphi_2, \Delta\varphi_3)$ in the M-coordinate system. The cylinder's orientation is represented by angles (ψ_1, ψ_2, ψ_3) with $\psi_1 = \varphi_1$, and a relationship between $(\Delta\psi_2, \Delta\psi_3)$ and $(\Delta\varphi_2, \Delta\varphi_3)$ given by (10).

Let $[x(t_0), y(t_0), z(t_0), u(t_0), v(t_0), w(t_0)]$ be the cylinder's initial translation and velocity and $[\psi_1(t_0), \psi_2(t_0), \psi_3(t_0), \omega_1(t_0), \omega_2(t_0), \omega_3(t_0)]$ be the cylinder's initial orientation and angular velocity. Following the procedures listed in Fig. 8, the values of these variables for next time step $(t = t_1)$ are calculated. Repeat of the procedures leads to predicting the cylinder's position and orientation as falling through the water column.

Theoretically, the model integration stops when the vertical coordinate of COM [i.e., $z(t)$ in the E-coordinate and the elevation angle $\psi_2(t)$ in the M-coordinate do not change with time (in the sediment column):

$$\frac{dz}{dt} = 0, \quad \frac{d\psi_2}{dt} = 0. \quad (88)$$

Practically, the following criteria are used to stop the integration,

$$\left| \frac{dz}{dt} \right| \leqslant \varepsilon_1, \quad \left| \frac{d\psi_2}{dt} \right| \leqslant \varepsilon_2, \quad (89)$$

where $(\varepsilon_1, \varepsilon_2)$ user-defined small values. In this study, we use

$$\varepsilon_1 = 10^{-6}\text{m}, \quad \varepsilon_2 = 10^{-4}.$$

8 Cylinder Drop Experiments

Two cylinder drop experiments were conducted to collect data for the model evaluation. Exp-1 was designed to collect data on a cylinder's motion in the water column for various combinations of the cylinder's parameters. Exp-2 was designed to collect synchronized data on sediment parameters (shear strength and density) and the cylinder's burial depth and orientation.

8.1 Exp-1. Exp-1 was conducted at the Naval Postgraduate School swimming pool in June 2001 [16]. It consisted of dropping each of three model cylinders (Fig. 9) into the water where each drop was recorded underwater from two viewpoints. The physical parameters of the model cylinders are listed in Table 2. Figure 10 depicts the overall setup. The controlled parameters for each drop were L/R ratio, χ-value, initial velocity $(\mathbf{V}_{\text{in}})$, and drop angle. The E-coordinate system is chosen with the origin at the corner of the swimming pool with the two sides as x and y axes and the vertical z axis. The initial injection of cylinders was in the (y,z) plane
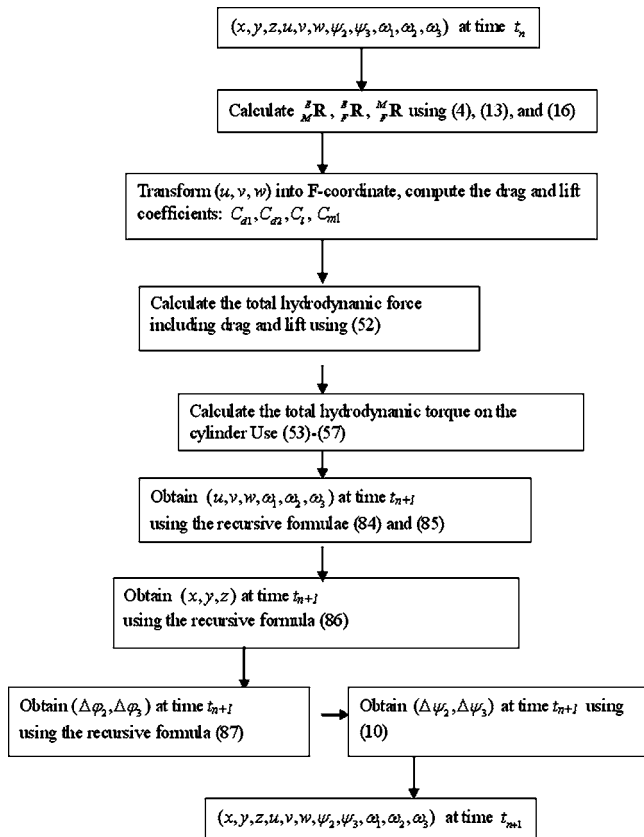
$(x, y, z, u, v, w, \psi_2, \psi_3, \alpha_1, \alpha_2, \alpha_3)$ at time t_n

Calculate $^B_M \mathbf{R}$, $^B_F \mathbf{R}$, $^M_F \mathbf{R}$ using (4), (13), and (16)

Transform (u, v, w) into F-coordinate, compute the drag and lift coefficients: $C_{d1}, C_{d2}, C_l, C_{ml}$

Calculate the total hydrodynamic force including drag and lift using (52)

Calculate the total hydrodynamic torque on the cylinder Use (53)-(57)

Obtain $(u, v, w, \alpha_1, \alpha_2, \alpha_3)$ at time t_{n+1} using the recursive formulae (84) and (85)

Obtain (x, y, z) at time t_{n+1} using the recursive formula (86)

Obtain $(\Delta\varphi_2, \Delta\varphi_3)$ at time t_{n+1} using the recursive formula (87)

Obtain $(\Delta\psi_2, \Delta\psi_3)$ at time t_{n+1} using (10)

$(x, y, z, u, v, w, \psi_2, \psi_3, \alpha_1, \alpha_2, \alpha_3)$ at time t_{n+1}

Fig. 8 Procedure of the recursive model

(Fig. 11).

Initial velocity ($\mathbf{V}_{in}$) was calculated by using the voltage return of an infrared photo detector located at the base of the cylinder injector. The infrared sensor produced a square wave pulse when no light was detected due to blockage caused by the cylinder's passage. The length of the square wave pulse was converted into time by using a universal counter. Dividing the cylinder's length by the universal counter's time yielded $\mathbf{V}_{in}$. The cylinders were dropped from several positions within the injector mechanism in order to produce a range of $\mathbf{V}_{in}$. The method used to determine $\mathbf{V}_{in}$ required that the infrared light sensor be located above the water's surface. This distance was held fixed throughout the experiment at 10 cm.

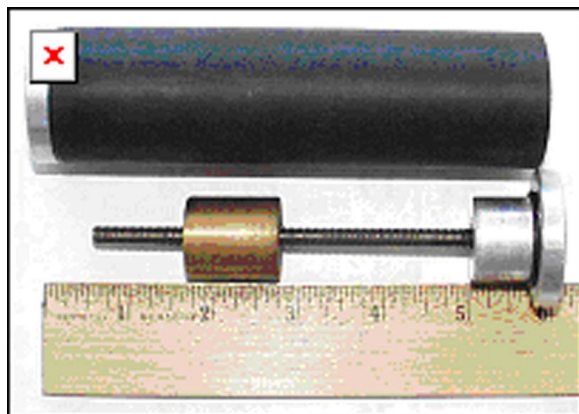The drop angle (initial value of $\psi_2^{(in)}$) was controlled using the

Fig. 9 Internal components of the model cylinder

Table 2 Physical parameters of the model cylinders

Cylinder	Mass (g)	L (cm)	Volume (cm^3)	ρ_m (g m^{-3})	J_1 (g m^2)	χ (cm)	$J_2(J_3)$ $\times$(g m^2)
1	322.5	15.20	191.01	1.69	330.5	0.00	6087.9
						0.74	5783.0
						1.48	6233.8
2	254.2	12.10	152.05	1.67	271.3	0.06	3424.6
						0.53	3206.5
						1.00	3312.6
3	215.3	9.12	114.61	1.88	235.0	0.00	1695.2
						0.29	1577.5
						0.58	1556.8

drop angle device. Five screw positions marked the 15 deg, 30 deg, 45 deg, 60 deg, and 75 deg. The drop angles were determined from the lay of the pool walkway, which was assumed to be parallel to the water's surface. A range of drop angles was chosen to represent the various entry angles that air- and surface-laid mines exhibit in naval operation. This range produced velocities whose horizontal and vertical components varied in magnitude. This allowed for comparison of cylinder trajectory sensitivity with the varying velocity components.

For each drop the cylinder was set to a χ value. For positive χ value, the cylinders were placed into the injector so that the COM was located below the geometric center. For negative χ value, the
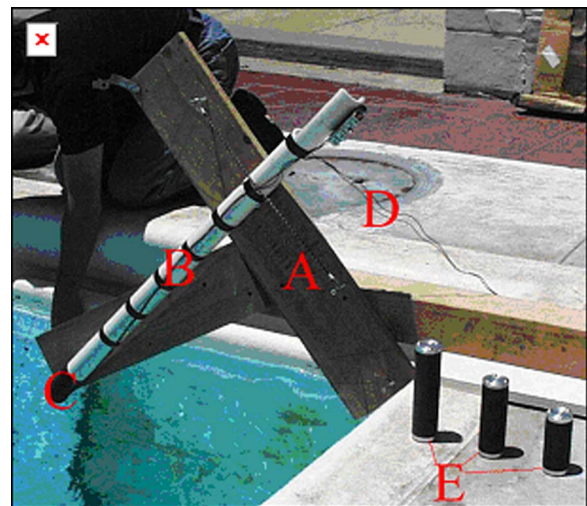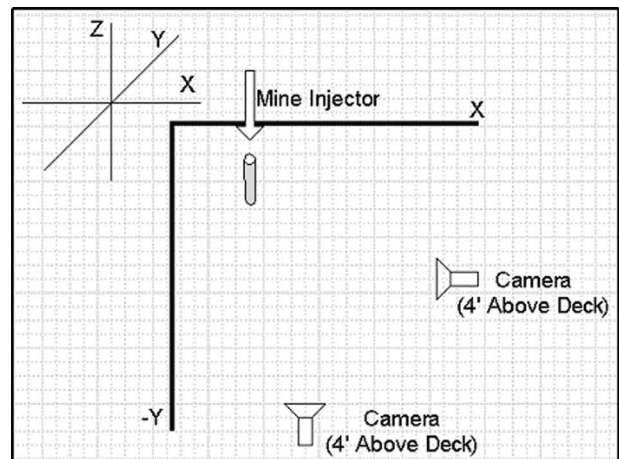

Fig. 10 Exp-1 equipments

Fig. 11 Top view of Exp-1

Journal of Applied Mechanics

Table 3 Number of drops conducted for different drop angles and χ values for $L/R=15/2$

$\psi_2^{(in)}$	15 deg	30 deg	45 deg	60 deg	75 deg
χ_2	13	15	15	15	12
χ_1	9	15	15	15	9
χ_0	12	14	15	18	6
χ_{-1}	0	6	6	6	0
χ_{-2}	2	6	6	0	0

Table 4 Measuring ranges of the gravity cores

Weight (g)	Apex-angle	Penetration (mm)	Undrained shear strength (kPa)
400	30 deg	4.0–15.0	25–1.8
100	30 deg	5.0–15.0	4–0.45
60	60 deg	5.0–15.0	0.6–0.067
10	60 deg	5.0–20.0	0.10–0.0063

COM was located above the geometric center to release. A series of drops was then conducted in order of decreasing mine length for each angle. Table 3 indicates number of drops conducted for different drop angles and χ value for $L/R=15/2$. The number of drops for other L/R ratios $(12/2, 9/2)$ is comparable to that for the L/R ratio of $15/2$. All together there were 712 drops. Each video camera had a film time of approximately 1 h. At the end of the day, the tapes were replayed in order to determine clarity and optimum camera position.

Upon completion of the drop phase, the video from each camera was converted to digital format. The digital video for each view was then analyzed frame by frame (30 Hz) in order to determine the mine's position in x-z and y-z planes. The cylinder's top and bottom positions were input into a MATLAB generated grid, similar to the ones within the pool. The first point to impact the water was always plotted first. This facilitated tracking of the initial entry point throughout the water column. The cameras were not time synchronized; thus, the first recorded position corresponded to when the full length of the mine was in view.

8.2 Exp-2. Exp-2 was conducted on the *R/V John Martin* on May 23, 2000 [17]. The barrel with density ratio of 1.8 was released horizontally while touching the surface. The initial conditions are

$$\mathbf{V}_{in}=0, \quad \psi_2^{(in)}=90°, \tag{90}$$

This would be to eliminate any chance of inertial effects caused by uneven introduction into the air-sea interface. This also set the initial velocity parameter in the code to zero. The barrel was to be released 17 times. The diver would snap the quick-release shackle on the barrel and then dive down to conduct measurements. The average depth of the water was 13 m. Since it was uncertain the path the barrel would follow, both the releasing diver and a second safety diver would stay on the surface until after the barrel had dropped. Once reaching the bottom, one diver would take penetration measurements using a meter stick marked at millimeter increments while the other would take a gravity core. After 17 drops, the divers began to run out of air and results were not varying greatly so the decision was made to end the experiment. Upon return to the Monterey Bay Aquarium Research Institute, the gravity cores were taken immediately to the USGS Laboratories in Menlo Park, CA where they were refrigerated until the analysis could be performed on May 31–June 1, 2000.

Analysis of the gravity cores was begun on May 31, 2000 at the USGS Laboratories in Menlo Park, CA. The gravity cores were sliced into 2 cm segments to a depth of 10 cms, and then sliced into 4 cm segments. A fall cone apparatus (Model G-200) was used to determine sediment density $\rho_s(z)$ and shear strength. In the test, it is assumed that the shear strength of sediment at constant penetration of a cone is directly proportional to the weight of the cone, and the relation between undrained shear strength s and the penetration h of a cone of weight Q is given by

$$S(z)=KQ/h^2, \tag{91}$$

where K is a constant which depends mainly on the angle of the cone, but is also influenced by the sensitivity of the clay/sediment. Four different cones are used with this instrument, each one hav-

ing the measuring range listed in Table 4. The cones are suspended from a permanent magnet. By pressing a knob, the magnet is moved so that the magnetic field is broken momentarily and the cone is released. Measurements are taken of penetration depth and the evolution is repeated five times per sediment slice. These values are then averaged and correlated with a table which gives shear strength. Previous studies [18] showed that the sediment parameters are the most critical element in determining how deep an object is buried when it came to rest. During the experiment at the Monterey Bay, we obtained 17 gravity cores. Sediment bulk density and shear strength profiles (Fig. 12) generally show increase with depth until approximately 6–9 cm below the water-sediment interface.

9 Model-Data Comparison

The U.S. Navy has a 2D model in the x-z plane (IMPACT28) to predict the cylinder's trajectory and impact burial. Since the motion of the cylinder is 3D, the impact burial prediction using the 2D model has large errors [19–21]. In this study, a new 3D model (called IMPACT35) is developed on the base of momentum balance $(19a)$ and $(19b)$ and moment of momentum balance (20) using a triple coordinate transform [8] and cylinder decomposition. To evaluate the value added to the 3D model, comparison among the observed data (from Exp-1 and Exp-2) and predicted data using 2D (IMPACT28) and 3D (IMPACT35) models is conducted. Since position and orientation of the cylinder were tape recorded after it is submerged into the water, the free water surface effect was not detected from Exp-1 and Exp-2.

9.1 Comparison Using Exp-1 Data. Improvement from IMPACT28 to IMPACT35 in predicting cylinders' trajectory and orientation in the water column is verified using the Exp-1 data. Here, we list two examples.

Positive χ **(Nose-Down):** Cylinder 1 ($L=15.20$ cm, $\rho=1.69$ g cm^{-3}) with $\chi=0.74$ cm is injected to the water with the
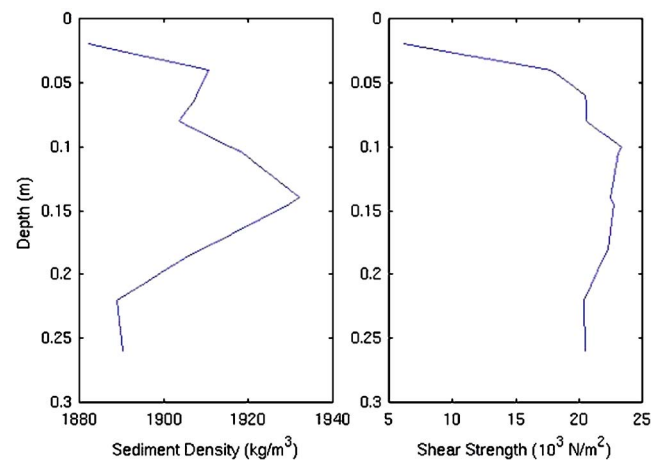

Fig. 12 Mean sediment density $\rho_s(z)$ and shear strength $S(z)$ profiles in the Monterey Bay collected during the cylinder drop experiment on May 31, 2000
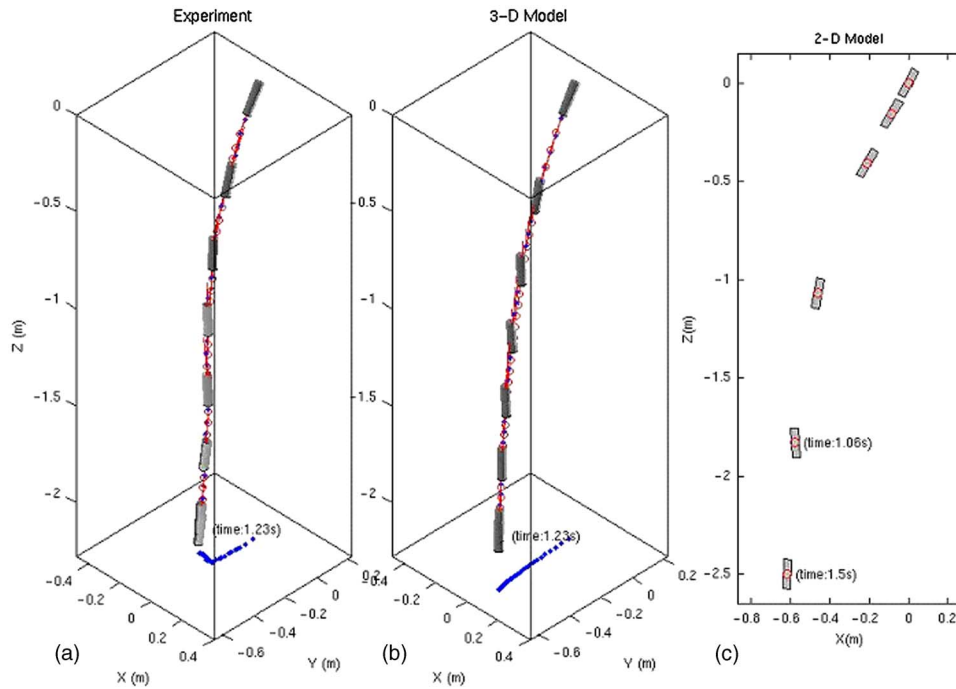
Fig. 13 Movement of cylinder 1 (L=15.20 cm, ρ=1.69 g cm^{-3}) with χ=0.74 m and drop angle 45 deg obtained from (*a*) experiment, (*b*) 3D IMPACT35 model, and (*c*) 2D Impact28 model

drop angle 45 deg. The physical parameters of this cylinder are given by

$$m = 322.5 \text{ g}, \quad J_1 = 330.5 \text{ g cm}^2, \quad J_2 = J_3 = 5783.0 \text{ g cm}^2. \tag{92a}$$

The initial conditions for the numerical models (IMPACT28 and IMPACT35) are taken the same as the experiment (see Sec. 8):

$$x_0 = 0, \quad y_0 = 0, \quad z_0 = 0, \quad u_0 = 0, \quad v_0 = -1.55 \text{ m s}^{-1},$$

$$w_0 = -2.52 \text{ m s}^{-1},$$

$$\psi_{10} = 0, \quad \psi_{20} = 60°, \quad \psi_{30} = -95°, \quad \omega_{10} = 0,$$

$$\omega_{20} = 0.49 \text{ s}^{-1}, \quad \omega_{30} = 0.29 \text{ s}^{-1}. \tag{92b}$$

Substitution of the model parameters (92*a*) and the initial conditions (92*b*) into IMPACT28 and IMPACT35 leads to the predictions of the cylinder's translation and orientation that are com-
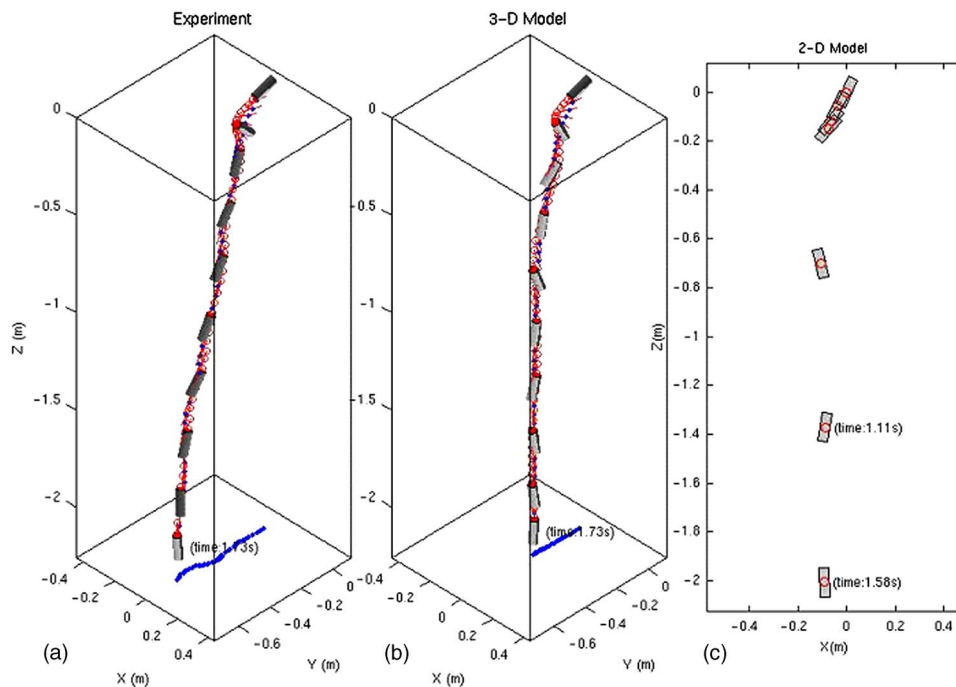

Fig. 14 Movement of cylinder 2 (L=12.10 cm, ρ=1.67 g cm^{-3}) with χ=−1.00 cm and drop angle 30 deg obtained from (*a*) experiment, (*b*) 3D IMPACT35 model, and (*c*) 2D Impact28 model

pared with the data collected during Exp-1 at time steps (Fig. 13). The new 3D model (IMPACT35) simulated trajectory agrees well with the observed trajectory. Both show the same slant-straight pattern and the same travel time (1.23 s) for the cylinder passing through the water column. However, the existing 2D model (IMPACT28) has less capability to predict the cylinder's movement in the water column. The travel time predicted by IMPACT28 is 1.5 s, much more than the observed value.

Negative χ **(Nose-Up):** Cylinder 2 ($L = 12.10$ cm, $\rho = 1.67$ g cm^{-3}) with $\chi = -1.00$ cm is injected to the water with the drop angle 30 deg. The physical parameters of this cylinder are given by

$$m = 254.2 \text{ g}, \quad J_1 = 271.3 \text{ g cm}^2, \quad J_2 = J_3 = 3312.6 \text{ g cm}^2. \tag{93a}$$

The initial conditions for the numerical models (IMPACT28 and IMPACT35) are taken the same as the experiment (see Sec. 8):

$$x_0 = 0, \quad y_0 = 0, \quad z_0 = 0, \quad u_0 = 0, \quad v_0 = -0.75 \text{ m s}^{-1},$$

$$w_0 = -0.67 \text{ m s}^{-1},$$

$$\psi_{10} = 0, \quad \psi_{20} = 24°, \quad \psi_{30} = -96°, \quad \omega_{10} = 0,$$

$$\omega_{20} = -5.08 \text{ s}^{-1}, \quad \omega_{30} = 0.15 \text{ s}^{-1}. \tag{93b}$$

The predicted cylinder's translation and orientation are compared with the data collected during Exp-1 at time steps (Fig. 14). The new 3D model (IMPACT35) simulated trajectory agrees well with the observed trajectory. Both show the same flip-spiral pattern and the same travel time (1.73 s) for the cylinder passing through the water column. The flip occurs at 0.11 s (0.13 s) after the cylinder enters the water in the experiment (IMPACT35). After the flip, the cylinder spirals down to the bottom. However, the existing 2D model (IMPACT28) does not predict the flip-spiral pattern.

9.2 Comparison Using Exp-2 Data. After running the two models (IMPACT35 and IMPACT28) for each gravity core regime $[\rho_s(z), S(z)]$ from the initial conditions (90), the burial depths were compared with measured burial depth data (Fig. 15). As evident, IMPACT35 improves the prediction capability. The existing 2D model (IMPACT25) overpredicts actual burial depth by an order of magnitude on average. However, the 3D model (IMPACT35) predicts the burial depth reasonably well without evident overprediction. Since the gravity cores were taken for approximately 2 to 3 m from the impact location, several cores were taken for each drop. This allowed an average to be calculated in order to yield more accurate data for each drop.

10 Conclusions

1. A 3D model (IMPACT35) is developed to predict the translation and orientation of a falling rigid cylinder through air, water, and sediment. It contains three components: triple coordinate transform, cylinder decomposition, and hydrodynamics of a falling rigid object in a single medium (air, water, or sediment) and in multiple media (air-water and water-sediment interfaces).

2. Triple coordinate transform is useful for modeling the movement of a rigid body in air-water-sediment. The body forces (including buoyancy force) and torques are represented in the E-coordinate system, the hydrodynamic forces (such as the drag and lift forces) and torques are represented in the F-coordinate, and the cylinder's moments of gyration are represented in the M-coordinate. The momentum (moment of momentum) equation for predicting the cylinder's translation velocity (orientation) is represented in the E-coordinate (M-coordinate) system. Transformations among the three coordinate systems are used to convert the forcing terms into E-coordinate (M-coordinate) for the momentum (moment of momentum) equation.
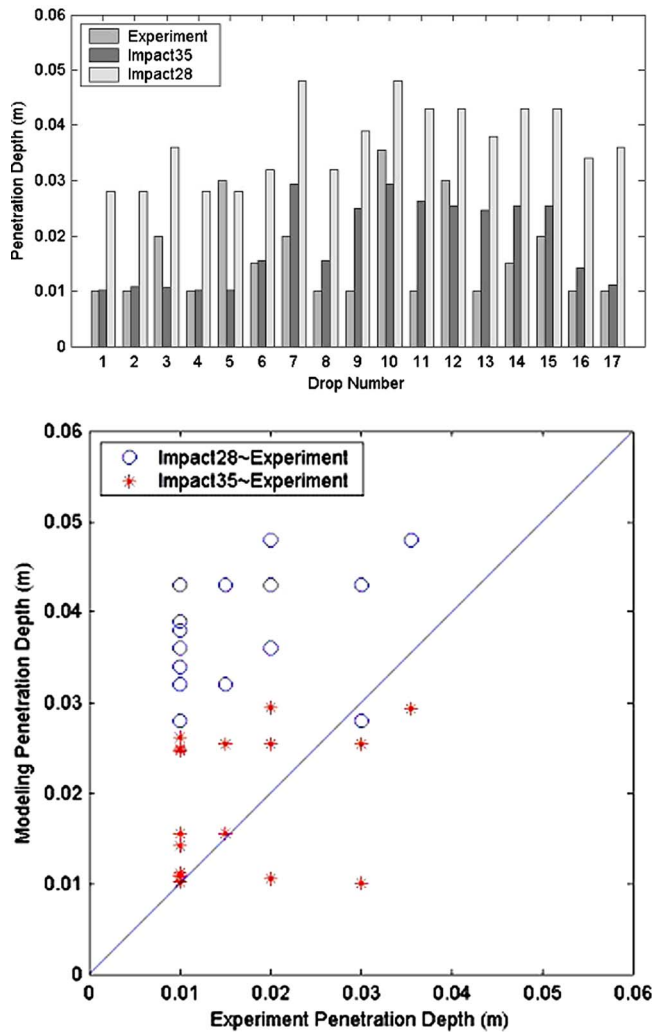
Fig. 15 Comparison among observed and predicted burial depths

3. During the penetration, the part that contacts the fluid (air or water) is treated as an equivalent cylinder with the same mass and PCOV location. The buoyancy and hydrodynamic forces and torques are computed in the equivalent cylinder. The procedure developed for calculating external forcing (buoyancy and hydrodynamic forces and torques) for a single cylinder is used for the equivalent cylinder.

4. Impact force and torque below the water-sediment interface are calculated on the basis of the fact that at the instance of penetration, the sediment exerts an impact force only on the portion of the cylinder's surface, which moves towards the sediment. The normal and tangential components of the impact force are calculated separately. The normal component is calculated using the sediment density and shear strength profiles. The tangential component is computed using the friction law between two solid bodies (i.e., proportional to the normal component). The torque is easily obtained after the impact force is determined.

5. The dynamic system for predicting trajectory and orientation of a rigid cylinder in air, water, and sediment are highly nonlinear. For example, the apparent torque in the moment of momentum equation (20) (represented in the F-coordinate) is nonlinear. The drag and lift forces are nonlinear terms which depend on the square of the fluid-to-body velocity. Two major assumptions are used to simplify the system. First, the apparent torque is neglected. Second, for

the given time step t_n, the nonlinear drag and lift forces and torques are linearized at any time instance with temporally varying coefficients (also dependent on the fluid-to-cylinder velocity) evaluated at the previous time step, t_{n-1}. With the given cylinder's parameters (translation, velocity, orientation, and angular velocity) at the time step t_n, $[x(t_n), y(t_n), z(t_n); u(t_n), v(t_n), w(t_n); \psi_1(t_n), \psi_2(t_n), \psi_3(t_n), \omega_1(t_n), \omega_2(t_n), \omega_3(t_n)]$, the model has analytical solutions at the time step t_{n+1}. The recursive procedure is established to predict the cylinder's translation, velocity, orientation, and angular velocity through air, water, and sediment from the initial conditions. The strength of such treatments guarantees the convergence of the model integration.

Since neglect of the apparent torque is feasible only for slow rotation around the cylinder's main axis (i.e., small self-spin angular velocity ω_1), and since local linearizations of drag and lift forces and torques are feasible for relatively small fluid-to-cylinder velocity, the model might not be valid if ω_1 or the fluid-to-cylinder velocity is large such as for fast water entry and fast self spinning. A fully numerical calculation (rather than the recursive procedure) should be developed for the prediction.

6. Two cylinder drop experiments were conducted to evaluate the 3D model. Model-data comparison shows that IM-PACT35 improves the prediction capability drastically with an order of error reduction in the cylinder burial depth, more accurate cylinder track (depth and orientation) prediction, and more accurate travel time of the cylinder through air-water-sediment.

Acknowledgment

Nomenclature

B = length of the sediment rupture line
(C_{d1}, C_{d2}) = drag coefficients along and across the cylinder
C_l = lift coefficient
C_{tl} = translational lift coefficient, kg s^{-1}
d = cylinder diameter, m
e_v = void ratio
(f_1, f_2, f_3) = added-mass ratios for drag and lift forces
f_r = added-mass ratio for moment of drag and lift forces
(f_{rd2}, f_{rd3}) = rotational drag force, N
$\mathbf{F}_b$ = buoyancy force, N
$\mathbf{F}_d$ = drag force, N
$(\mathbf{F}_{d1}, \mathbf{F}_{d2}, \mathbf{F}_{d3})$ = drag force in the F-coordinate, N
$\mathbf{F}_l$ = lift force, N
$(\mathbf{F}_{l1}, \mathbf{F}_{l2}, \mathbf{F}_{l3})$ = lift force in the F-coordinate, N
$\mathbf{F}_{pw}$ = pore water pressure force, N
$(\mathbf{i}_E, \mathbf{j}_E, \mathbf{k}_E)$ = unit vectors in the E-coordinate
$(\mathbf{i}_F, \mathbf{j}_F, \mathbf{k}_F)$ = unit vectors in the F-coordinate
$(\mathbf{i}_M, \mathbf{j}_M, \mathbf{k}_M)$ = unit vectors in the M-coordinate
(J_1, J_2, J_3) = moments of gyration, kg m^2
$(J_1^{(i)}, J_2^{(i)}, J_3^{(i)})$ = moments of gyration for cylindrical part i, kg m^2
k_p = permeability coefficient, m s^{-1}
L = length of the cylinder, m
(l_1, l_2, l_3) = lengths of the cylindrical Parts, m
$(m_1, \ldots, m_6)$ = masses of cylindrical parts, kg
$\mathbf{M}_b$ = torque due to the buoyancy force, kg m^2 s^{-2}

$\mathbf{M}_h$ = torque due to the hydrodynamic force, kg m^2 s^{-2}
$(\mathbf{M}_{d1}, \mathbf{M}_{d2}, \mathbf{M}_{d3})$ = torques due to the drag force in the M-coordinate, kg m^2 s^{-2}
$\mathbf{r}$ = position vector (in the M-coordinate) of point on the cylinder's surface
$\mathbf{r}_{pw}$ = position vector (in the M-coordinate) indicating the location of the cylinder's rupture line
R = radius of the cylinder
(R_1, R_2, R_3) = radii of cylindrical parts, m
Re = Reynolds number
$\mathbf{V}$ = translation velocity, m s^{-1}
$\mathbf{V}_r$ = water-to-cylinder velocity, m s^{-1}
$\mathbf{V}_1$ = component of $\mathbf{V}_r$ along the cylinder, m s^{-1}
$\mathbf{V}_2$ = component of $\mathbf{V}_r$ perpendicular to the cylinder, m s^{-1}
$\mathbf{V}_w$ = water velocity (m s^{-1})
$V^{(in)}$ = initial speed of dropping cylinder, m s^{-1}
ν = molecular viscosity of the water, m^{2}s^{-1}
Π = volume of the cylinder, m^3
ρ = density of the cylinder kg m^{-3}
ρ_w = density of the water, kg m^{-3}
χ = distance between COM and COV, m
(ψ_1, ψ_2, ψ_3) = angles determining the cylinders' orientation
$\boldsymbol{\omega}$ = angular velocity, s^{-1}
$(\omega_1, \omega_2, \omega_3)$ = angular velocity components in the M-coordinate, s^{-1}
$(\omega_1^F, \omega_2^F, \omega_3^F)$ = angular velocity components in the F-coordinate, s^{-1}

References

[1] White, F. M., 1974, *Viscous Fluid Flow*, McGraw-Hill, New York.
[2] Boorda, J. M., 1999, "Mine Countermeasures - An Integral Part of Our Strategy and Our Forces," *Federation of American Scientists*, Washington DC (http://www.fas.org/man/dod-101/sys/ship/weaps/docs/cnopaper.htm).
[3] Inman, D. L., and Jenkins, S. A., 2002, "Scour and Burial of Bottom Mines, a Primer for Fleet Use. University of California, San Diego," *SIO Reference Series 02-8*, Scripps Institution of Oceanography, University of California, San Diego, CA.
[4] Inman, D. L., and Jenkins, S. A., 2005, "Scour and burial of objects in shallow water," *Encyclopedia of Coastal Science*, M. Schwartz, ed., Springer, New York.
[5] Rennie, S., Brandt, A., and Plant, N. 2004, "Utilization of an Expert System for Predicting Mine Burial: Quantifying Uncertainty," *Proceedings of Sixth International Symposium on Technology and the Mine Problem*, Naval Postgraduate School, Monterey, CA, May 10–13, DVD-Rom.
[6] Haeger, S., 2004, "Operational Ocean Modeling Support for Mine Warfare in Operation Iraqi Freedom," *Proceedings of Sixth International Symposium on Technology and the Mine Problem*, Naval Postgraduate School, Monterey, CA, May 10–13, DVD-Rom.
[7] Elmore, P. A., and Richardson, M. D., 2004, "Regional Mine Burial Prediction Using Monte Carlo and Deterministic Methods," *Proceedings of Sixth International Symposium on Technology and the Mine Problem*, Naval Postgraduate School, Monterey, CA, May 10-13, DVD-Rom.
[8] Chu, P. C., Fan, C. W., Evans, A. D., and Gilles, A. F., 2004, "Triple Coordinate Transforms for Prediction of Falling Cylinder Through the Water Column," ASME J. Appl. Mech., **71**, pp. 292–298.
[9] Crowe, C. T., Roberson, J. A., and Elger, D. F., 2001, *Engineering Fluid Mechanics*, 7th ed., John Wiley & Sons, New York.
[10] Rouse, H., 1938, *Fluid Mechanics for Hydraulic Engineers*, 1st ed., McGraw-Hill, New York.
[11] Von Mises, R., 1959, *Theory of Flight*, 1st ed., Dover, New York, pp. 564–585.
[12] Sumer, B. M., and Fredsøe, J., 1997, *Hydrodynamics Around Cylindrical Structures*, 1st ed., World Scientific, Singapore.
[13] Palmer, A., 1997, "Speed Effect in Cutting and Ploughing," Geotechnique, **49**(3), pp. 285–294.
[14] Simonsen, B. C., and Hansen, N. E. O., 1998, "Protection of Marine Structures by Artificial Islands," *Ship Collision Analysis*, H. Gluver and D. Olsen, eds.,

Balkema, Rotterdam, pp. 201–215.

[15] Hansen, N. E. O, Simonsen, B. C., and Sterndorff, M. J., 1994, "Soil Mechanics of Ship Beaching," *Proceedings on 24th International Conference on Coastal Engineering*, Kobe, Japan, pp. 3030–3044.

[16] Gilles, A. F., 2001, "Mine Drop Experiment," M.S. thesis, Naval Postgraduate School, Monterey, CA, p. 151.

[17] Smith, T. B., 2000. "Validation of the Mine Impact Burial Model Using Experimental Data," M.S. thesis, Naval Postgraduate School, Monterey, CA, p. 156.

[18] Chu, P. C., Gilles, A. F., Fan, C., and Fleischer, P., 2002, "Hydrodynamical Characteristics of a Falling Cylinder in the Water Column," *Advances in Fluid Mechanics*, M. Rahman, R. Verhoeven, and C. A. Brebbia, eds., WIT Press, Southampton, **4**, pp. 163–181.

[19] Taber, V. L., 1999, "Environmental Sensitivity Studies on Mine Impact Burial Prediction Model," M.S. thesis, Naval Postgraduate School, Monterey, CA, p. 50.

[20] Evans, A., 2002, "Hydrodynamics of Mine Impact Burial," M.S. thesis, Naval Postgraduate School, Monterey, CA, p. 470.

[21] Chu, P. C., Gilles, A. F., and Fan, C. W., 2005, "Experiment of Falling Cylinder Through the Water Column," Exp. Therm. Fluid Sci., **29**, pp. 555–568.